Extreme precipitation in Central Norway

A case and climate study

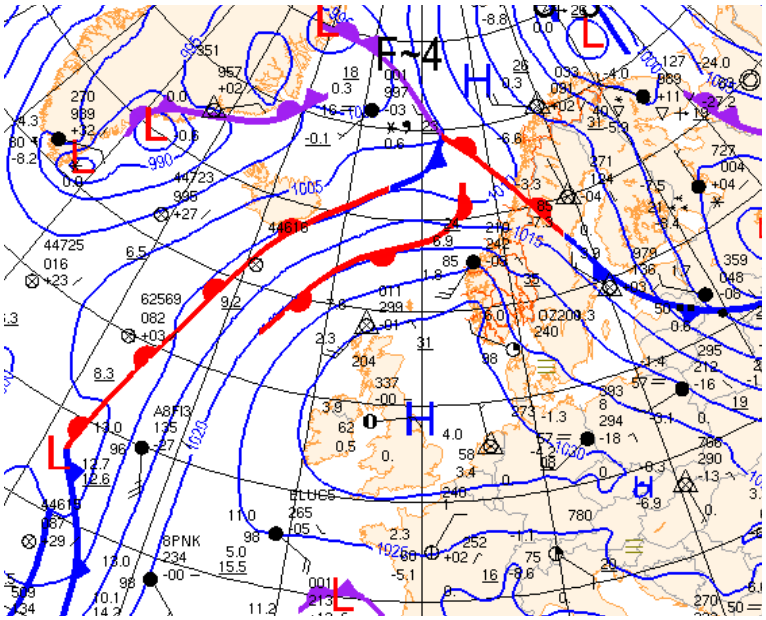

Master Thesis in Meteorology

Birthe Marie Steensen

June 2010

UNIVERSITY OF BERGEN
GEOPHYSICAL INSTITUTE

The figure on the front page shows
the surface analysis done by the
Norwegian Meteorological Institute
for 12 UTC 30 January 2006.

Acknowledgement

I would like to give my utmost gratitude to my supervisor Haraldur Ólafsson. I have appreciated all of his advice and encouragements. Due to his arrangement I had the opportunity to go to Iceland to work for a week and do other tourist activities. It is also due to Haraldur's initiative that I had two posters at EGU 2010, which he also presented for me, in addition to an attendance at the NMM 2010 in Helsinki.

I would like to thank Dag Kvamme at the Norwegian Meteorology Institute for his idea to study this extreme precipitation event.

Marius O. Jonassen for helping me with the modeling and other technical problems that may have occurred during my work. Thank you very much.

I am grateful for the precipitation data from satellite observations provided to me by Axel Andersson, and the gridded precipitation maps provided by Matthias Mohr.

Sigbjørn Grønås for reading my thesis and his useful comments.

At last I would like to thank my fellow students, they have probably been the best group of people to share this experience with, my sailing team, and most off all to my family for supporting me trough my whole education and especially during this last work on the thesis.

Abstract

An extreme precipitation event occurred over Central Norway at the end of January to the beginning of February 2006. The heavy precipitation in addition to high temperatures lead to snow melt and increased run-off, which produced flooding and landslides that caused considerable damage to infrastructure and loss of human life. A numerical weather prediction tool is used to model the flow pattern on synoptic and mesoscale to find the cause for the generation of the high precipitation rates. Forced lifting of warm moist air due to strong perpendicular winds over the mountains in Central Norway is found to be the main cause. A second topographical effect is the blocking of the flow by the mountain ridge in Southern Norway. The blocking causes a deflection and enhancement of the forcing over Central Norway, and leads to more precipitation. Vertical motion described by the quasi-geastrophic theory is found to be of limited importance. The warm moist air over Trøndelag during the event is calculated backwards to the subtropics. An investigation of the predictability of the event reveals a sensitivity in a baroclinic zone in an area south of Newfoundland upstream of the event. A likely effect of the global climate change is a shift in the frequency of extreme events, and an increase in combined extreme events like the one described in this thesis. Results from a global climate model are downscaled with a higher resolution regional climate model in order to acquire a description of the frequency of similar events in a future greenhouse gas scenario. There is found an increase in high temperature events during winter, and an increase in frequency for similar extreme precipitation events during the whole year and winter.

Contents

Chapter 1

Introduction

From 29 January to 2 February 2006 Central Norway experienced heavy precipitation. The weather situation caused snow melting which increased the run-off. This produced landslides and flooding that caused large damage to infrastructure, buildings and loss of human life. The cost of the flood is estimated to be around 80 million Norwegian kroner, and there were reported 449 damages to the insurance companies[1]. This is one of the most expensive flooding events reported in Norway.

An 'extreme weather' warning is issued by the Norwegian Meteorological Institute if there is a risk of damage to infrastructure, buildings or risk of human life due to the weather conditions. The warning is issued when the predicted wind force is adequately strong, or there is expected extreme precipitation that can produce flooding. The impact of the extreme weather also has to affect a larger area like a county. The extreme weather warning is first distributed to the Norwegian Water Resources and Energy Directory, then the Ministry of Justice, in addition to the County Governor in the affected counties in order to minimize the damages. Notification trough media or telephone is also used when needed to alert people that are affected by the extreme weather. The 2006 extreme winter precipitation event did however not get an extreme weather warning.

Wintertime precipitation over Scandinavia and the North Atlantic Oscillation (NAO) are strongly related (Hurrell, 1995). Uvo (2003) shows that there is a positive variance explained by the NAO-index in wintertime precipitation over Central Norway. Increased precipitation amounts in most areas of Norway during the last century can partly be explained with a corresponding positive trend in the NAO (Hanssen-Bauer & Førland, 1998). Alfnes & Førland (2006) shows that the frequency of heavy precip-

[1]The Norwegian trade organization for insurance companies, Finance Norway (FNO, 2010)

itation events in Norway also have increased during the 20th century.

Events combined of both heavy precipitation and high temperatures during winter and spring that lead to snow-melt and thus increased run-off and flooding, like this event, are often referred to as 'complex extremes' in climate studies (IPCC, 2001). Due to the ongoing increase in greenhouse gases there is predicted a further intensification in the hydrological cycle, and an increase in such complex extremes.

There are several studies done on the effects of global climate change over Norway. The studies find that the warming trend is strongest during winter (Hanssen-Bauer *et al.*, 2005; Haugen & Iversen, 2008). There is also expected an increase in rainfall, both in rainfall intensities and in the frequency of rainfall events (Beldring *et al.*, 2008). Benestad & Haugen (2007) studies combined temperature and precipitation events during winter and spring for a future climate scenario, but few other studies are done on events that can lead to complex extremes. The paper concludes that high-rainfall-high-temperature events can occur more frequently in the future, and thus increase the risk of flooding.

Given these observed and predicted trends, it is important to understand the relevant precipitation processes under extreme precipitation events. In this thesis the wintertime extreme precipitation event over Central Norway described above is studied. The study is presented in a paper in Chapter 7. The event is explored by conventional data, data from remote sensing and numerical simulations.

In Chapter 2, theory used in the study is described. The numerical weather prediction tool used for studying the synoptic and meso scale flow pattern during the event, the Weather Research and Forecasting (WRF) model, are described in Chapter 3. The data used in the study are described in Chapter 4. In Chapter 5 the synoptic situation and observations from the event are presented and described.

In Chapter 6 a climate study on similar extreme precipitation events is presented. Modeled climate data for a control and future greenhouse gas scenario are downscaled by a regional climate model to values representing Ørlandet station. There values are compared with observed data from Ørlandet. Combined events of both high temperatures and strong westerly winds which can produce similar events are studied to find if there is a possibility the global warming will increase the frequency of events like the one described in this study in the future simulations. I the two last chapters, Chapter 8 and 9 a summary and general conclusions and some future work is included. Synoptic maps over the period in included in Appendix A.

Chapter 2

Theory

2.1 Vertical motion

A rising air parcel will undergo expansion due to lower pressure higher up in the atmosphere. The expansion leads to a decrease in temperature, this is called adiabatic cooling. When the water in the air parcel no longer can stay in the vapor face because of the temperature decrease, small water or ice particles are formed. These small particles are called hydrometeors, if they continue to grow they can become too heavy and fall to the ground as snow or rain.

2.1.1 Omega equation

The ω-equation estimates the large-scale vertical motion by using the vorticity and thermodynamic equations and quasi-geostrophic theory, (Holton, 2004).

$$\left(\nabla^2 + \frac{f_0^2}{\sigma}\frac{\partial^2}{\partial p^2}\right)\omega \approx \frac{f_0}{\sigma}\left[\frac{\partial \mathbf{V}_g}{\partial p} \bullet \nabla\left(\frac{1}{f_0}\nabla^2\Phi + f\right)\right] \tag{2.1}$$

Equation 2.1 show the diagnostic ω-equation for the instantaneous geopotential (Φ) field for adiabatic flow. σ is the stability parameter and f is the Coriolis parameter. ω is inversely proportional to the vertical velocity w, so $\omega > 0$ implies downward motion.

The right-hand side of Equation 2.1 describes the advection of absolute vorticity by

the thermal wind. Decreasing vorticity implies incresing thickness between pressure surfaces in higher and lower levels, if there is no temperature advection, a warming of the atmosphere is done by a descending motion described by the ω-equation. The same yields the other way, a declination motion will result if there is a warm air advection and no change in the vorticity field. In low-pressure systems where there is a decrease in vorticity in higher levels and no temperature advection in lower levels because of the surface low, the cooling of the atmosphere is done by an ascending motion which causes adiabatic cooling of the air parcels.

2.1.2 Forced ascent

Forced vertical motion due to topography can cause enhanced precipitation on the upwind side of a mountain ridge. The vertical velocity w can be estimated by using half of the length of the ridge the flows need to get over (L), the horizontal wind speed (U), and the mountain height (h). If the upstream horizontal wind is defined as $U = \frac{L}{t}$ and $w = \frac{h}{t}$, then the vertical velocity can be written as a function of h, U and L

$$w = \frac{hU}{L} \tag{2.2}$$

The vertical wind speed increases with U and the steepness of the mountain. The terrain-forced ascent will adiabatically cool the air and cause condensation and sometimes precipitation, see Figure 2.1. A simple equation from Smith (1979) shows that the precipitation is proportional to the slope of the mountain (α), the horizontal wind and saturation water vapor density (ρ_{w_s}):

$$R = \alpha U \rho_{w_s}(0), \tag{2.3}$$

where R is the precipitation intensity in $[\frac{kg}{m^2/sec}]$. Normally hydrometeor formation takes longer time than the typical values calculated by using this equation. There is no constant time scale for hydrometeor formation, since the accretion processes is nonlinear and different for snow and rain (Jiang & Smith, 2003). Precipitation due only to topography is therefore unlikely to occur, high terrain seems to enhance precipitation but not act as its sole cause.

Bergeron (1960) suggests an idealized two-cloud system for induced orographic precipitation called "seeder-feeder", see Figure 2.2. The upper seeder cloud is presumed

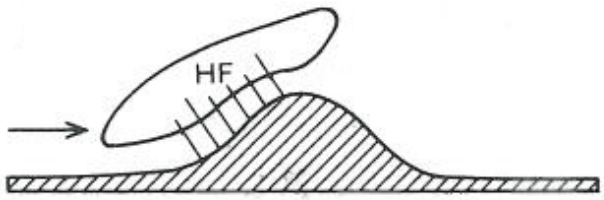

Figure 2.1: Orographic induced precipitation by forced ascent, Hydrometeor Formation (HF), from Smith (1989)

to be precipitating without topographic influence, the precipitation gets evaporated in lower levels so that this air becomes moister. When this air is lifted by the terrain it reaches supersaturation quickly and the feeder cloud is formed. The feeder cloud grows by collecting hydrometeors from the seeder cloud and the enlarged droplets may lead to drop splitting and even more droplets. In practice the two clouds may be combined into one or the seeder cloud can be influenced by the topography as well.

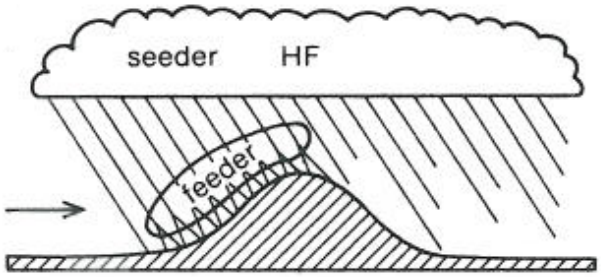

Figure 2.2: The "seeder-feeder" mechanism, from Smith (1989)

2.2 Mountain flow

A nondimensional mountain height can be defined as

$$\hat{h} = \frac{hN}{U} \tag{2.4}$$

where N is the Brunt-Väisälä frequency. The Brunt-Väisälä frequency describes the buoyancy on an vertically displaced air parcel, $N = \sqrt{\frac{g}{\theta}\frac{d\theta}{dz}}$. For $N^2 > 0$ the atmosphere is statically stable, and N is the frequency of the oscillation the air parcel has over its initial position. For $N^2 < 0$ the atmosphere is statically unstable, and the air parcel has an acceleration away from its initial position.

The pattern of the flow as it impinges the mountain depends on the nondimensional

mountain height. For low $\hat{h}$ the flow goes over the mountain, and the topography effect is big. When the mountain height or the atmospheric stability increases, the flow gets blocked by the mountain. The flow over the mountain will decrease, but the flow on the sides will increase because the flow will now try no move around the mountain instead of over it (e.g. Pierrehumbert & Wyman (1985); Ólafsson & Bougeault (1996)).

For large mountain ranges, rotational effects are also important. The Rossby number $R = \frac{U}{fL}$, where f is the Coriolis parameter, parameterizes the importance of this effect. The Coriolis force disrupts the symmetry of the flow around a mountain, and diverts the flow to the left side, facing downwind (e.g. Ólafsson (2000)). Another factor of the rotation is that as the flow approaches the mountain, the air flow rises on the left side as well. This contributes to systematically wetter weather on the left side of mountain ranges in the northern hemisphere (Hunt *et al.*, 2001).

2.3 Precipitation in Norway

The climate in Norway is highly affected by the position in the westerlies, the climate is wet and the winters are warmer than other parts of the World on the same latitude. The precipitation in Norway can roughly be divided into three types, frontal, orographic, and convective precipitation. In Central Norway during winter, precipitation is generally associated with synoptic scale fronts following extratropical cyclones.

Orographic precipitation enhancement occurs on the windward side of the mountains. In Norway, and in some other parts of the world this can be used to see the prevailing wind direction (Smith, 1989). Over Norway the annual mean precipitation is highest around west-facing mountains, see Figure 2.3. The topography in Southern Norway influences the precipitation distribution for warm front, occlusions, instability showers, and tropical warm air comming from the west over the Atlantic Ocean and invading the western coast of Norway (Spinnangr, 1943a,b; Spinnangr & Johansen, 1954).

During the last century Norway has experienced two warming periods, the first from the beginning of the century to 1940, and a second warming period from 1970 and up to precent date, (Hanssen-Bauer & Nordli, 1998). The second period can be associated with the strengthening of the average westerly winds over Norway, and especially during winter. This strengthening can be caused by natural variability, or it can be a response to the global warming that, in some climate models intensifies the storm track over Northern Europe (Ulbrich & Cristoph, 1999; Hanssen-Bauer & Førland, 2000). The mean annual precipitation during the second warming period has also increased with between 5 - 15 % in the majority of Norway (Hanssen-Bauer & Førland, 1998). This

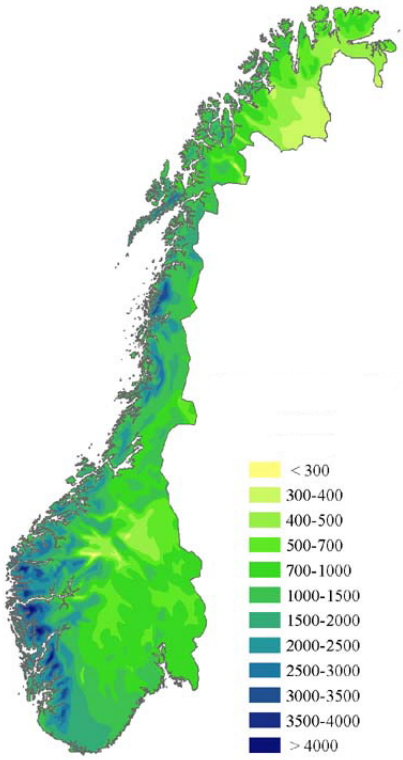

Figure 2.3: Mean annual precipitation for Noray during 1961-1990 (mm/year). From the Norwegian Meteorological Institute climate department (met.no/Klima). Areas that experience the most precipitation in blue are situated on the western coast of Norway.

increase is in consistency with the intensification of the storm track, which affects Norway especially due to its geographical position. The annual mean precipitation in Norway is predicted to further increase in the future due to the global warming and the intensification of the hydrological cycle (Hanssen-Bauer *et al.*, 2003; Haugen & Iversen, 2008; Beldring *et al.*, 2008).

2.3.1 Extreme precipitation

The station in Norway with the highest measured 24 hours accumulated precipitation is Indre Matre. The record is 229.6 mm/24h at 06 UTC on 26 November 1940 (Mamen, 2008). The station is situated in Western Norway, in the inner parts of Masfjorden to the north of Bergen. The station is highly affected by topographical effects. The synoptic situation on the 26 November 1940 was characterized by a stable persistent high-pressure over the bay of Biscay. To the north of this high-pressure, low-pressures and frontal systems moved towards Western Norway.

An extreme precipitation event over the area around Bergen described in literature are

a period during September 2005 in Stohl *et al.* (2008). The precipitation was caused by two former hurricanes transforming into extratropical cyclones. The cyclones brought with them warm moist air that was triggered by the topography on the Norwegian southwest coast and produced heavy precipitation. Figure 2.4 shows the 12 day trajectories calculated backwards between 00 UTC to 06 UTC on 14 September 2005. The trajectories are color coded according to the change of specific humidity, and show a humidity loss near the coast of Western Norway and a gain over the (sub)-tropical parts of the North Atlantic Ocean.

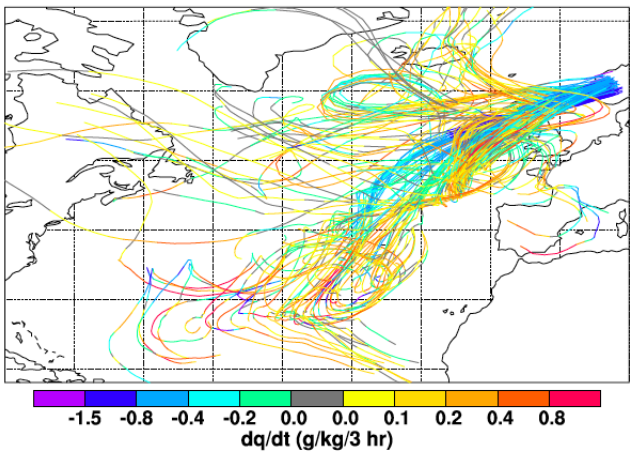

Figure 2.4: Trajectories calculated backwards over 12 days between 00 UTC to 06 UTC 14 September, from Stohl *et al.* (2008).

During the autumn of 2006, between 13 to 15 November, Western Norway experienced another extreme precipitation event. The event happened during a measurement campaign on the island Stord, situated on the western coast of Norway, described in Reuder *et al.* (2007). During the 14 November fronts in connection with a low-pressure system pass over Southern Norway. This lead to exceptionally high precipitation amounts, up to 240 mm in less than 24 hours were measured on the island on 14 November 2006.

An extreme precipitation event during August 2003 over Central Norway is described by Einarsson *et al.* (2004). The heavy precipitation was caused by a deep cyclone over southern Scandinavia. The precipitation in this case is also affected by the topography on the western coast of Norway, this is consistent with Figure 2.3.

Chapter 3

The numerical model

3.1 The Weather Research and Forecasting Model

The Weather Research and Forecasting Model (WRF) is a numerical weather prediction (NWP) tool and a atmospheric simulation system used in both research and operational forecasting. The WRF model is developed in collaboration with the National Center for Atmospheric Research (NCAR), the Mesoscale and Microscale Meteorology (MMM) Division, the National Oceanic and Atmospheric Administration's (NOAA), the National Centers for Environmental Prediction (NCEP), and the Earth System Research Laboratory (ESRL) among several other organizations. For more information see Skamarock (2008).

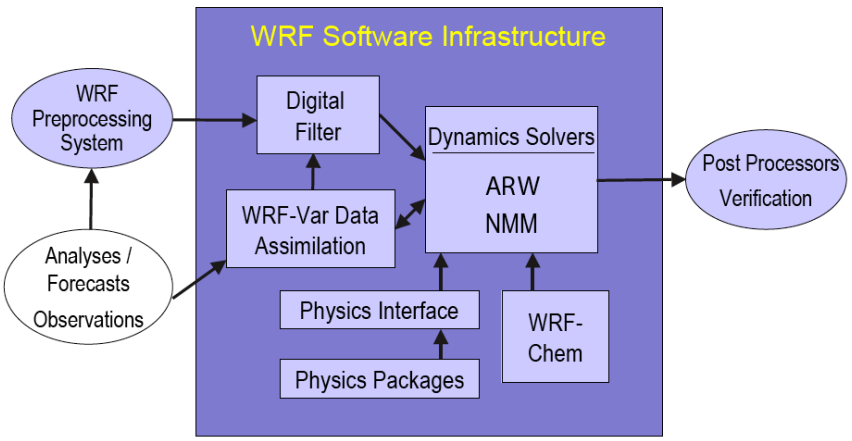

Figure 3.1: WRF system components, from Skamarock (2008)

Figure 3.1 shows the different system components. There are two dynamic solvers in the WRF software framework, the Advanced Research WRF (ARW) solver developed primarily at NCAR, and the Nonhydrostatic Mesoscale Model (NMM). In this study WRF version 3.0.1 with the ARW dynamic solver version 3 is used.

3.1.1 Governing equations

The ARW dynamic solver integrates the compressible, nonhydrostatic Euler equations. The equations are expressed by using a terrain-following mass vertical coordinate η (Laprise, 1992) that is defined as

$$\eta = (p_h - p_{ht})/\mu \quad \text{where} \quad \mu = p_{hs} - p_{ht} \tag{3.1}$$

p_h is the hydrostatic component of pressure, p_{hs} and p_{ht} are the hydrostatic pressure component along the surface and top boundaries, respectively (see Figure 3.2). η varies between 0 at the upper boundary and 1 at the surface boundary of the model's vertical domain.

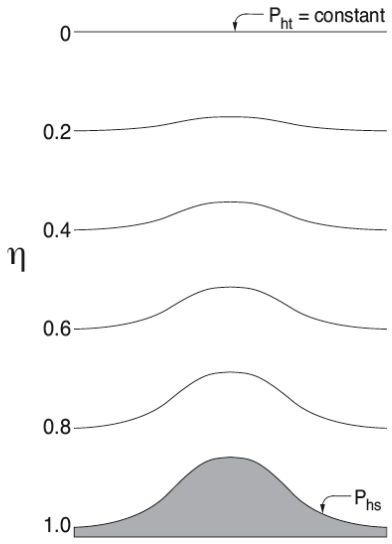

Figure 3.2: ARW vertical coordinate, (Skamarock, 2008)

When $\mu(x, y)$ are the mass per unit area within the column in the model domain at (x, y) the flux form of the variables can be written

$$\mathbf{V} = \mu\mathbf{v} = (U, V, W), \quad \Omega = \mu\dot{\eta}, \quad \Theta = \mu\theta \tag{3.2}$$

$\mathbf{v} = (u, v, w)$ are the covariant velocities in 3 dimensions. $\omega = \dot{\eta}$ is the contravariant 'vertical' velocity, θ is the potential temperature. In addition the geopotential is $\phi = gz$, the pressure is p, and $\alpha = 1/\rho$ is the inverse density. Using these definitions the Euler equations on flux-form can be formulated as:

$$\partial_t U + (\nabla \cdot \mathbf{V}u) - \partial_x(p\partial_\eta\phi) + \partial_\eta(p\partial_x\phi) = F_U \tag{3.3}$$

$$\partial_t V + (\nabla \cdot \mathbf{V}v) - \partial_y(p\partial_\eta\phi) + \partial_\eta(p\partial_y\phi) = F_V \tag{3.4}$$

$$\partial_t W + (\nabla \cdot \mathbf{V}w) - g(\partial_\eta p - \mu) = F_W \tag{3.5}$$

$$\partial_t \Theta + (\nabla \cdot \mathbf{v}\theta) = F_\Theta \tag{3.6}$$

$$\partial_t \mu + (\nabla \cdot \mathbf{V}) = 0 \tag{3.7}$$

$$\partial_t \phi + \mu^{-1}[(\mathbf{V} \cdot \nabla\phi) - gW)] = 0 \tag{3.8}$$

The diagnostic relation for inverse density

$$\partial_\eta\phi = -\alpha\mu \tag{3.9}$$

The equation of state

$$p = p_0(R_d\theta/p_0\alpha)^\gamma \tag{3.10}$$

In the equations 3.3 - 3.10, the subscripts x, y and η denote the differentiation

$$\nabla \cdot \mathbf{V}a = \partial_x(Ua) + \partial_y(Va) + \partial_\eta(\Omega a) \tag{3.11}$$

$$\mathbf{V} \cdot \nabla a = U\partial_x a + V\partial_y a + \Omega\partial_\eta a \tag{3.12}$$

where a is an arbitrary variable, $\gamma = c_p/c_v = 1.4$ is the ratio of the heat capacities for dry air, R_d is the gas constant for dry air, and p_0 is the reference pressure. Due to the

model's parameterization of the physics, turbulent mixing, spherical projections, and the Earth's rotation, the terms F_U, F_V, F_W and F_Θ arises. The equations 3.3 - 3.8 are prognostic, while the two latter (3.9 - 3.10) are diagnostic equations and describes the atmosphere.

In the final form of the equations (not shown), the effects of moisture in the atmosphere and map factors like map projection, Coriolis, and curvature terms are included. Perturbation variables are also defined to reduce truncation errors.

3.1.2 Space and temporal discretization

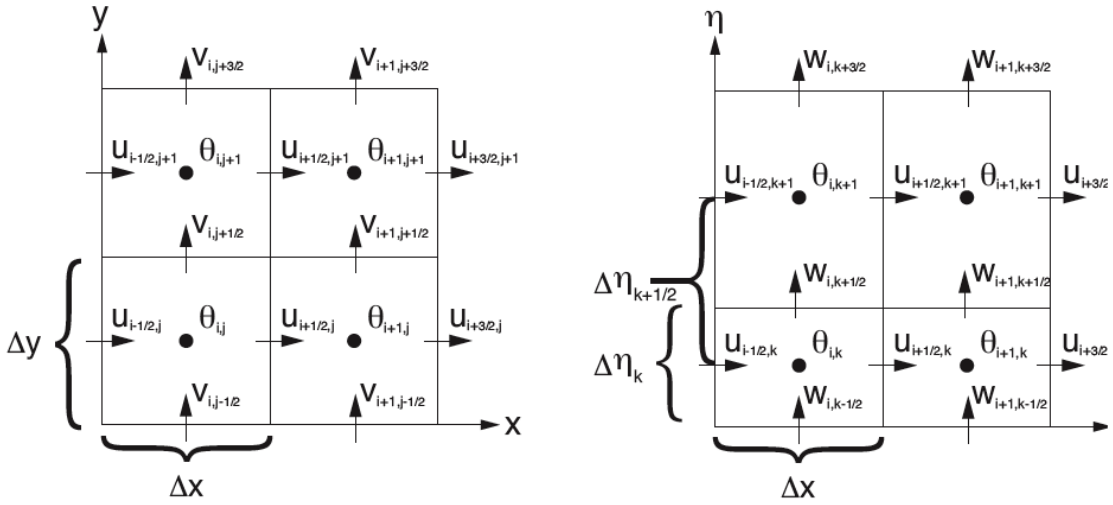

(a) Horizondal grid **(b)** Vertical grid

Figure 3.3: The horizontal and vertical grids used by the ARW solver, Skamarock (2008).

The ARW solver uses an Arakawa C grid staggering, where the mass points and velocity points have a half grid length between them, see Figure 3.3. θ are located at the mass points, and the wind vectors u, v and w are located at the u points, v points, and w points, respectively. In addition to what is shown on the Figure, the column mass μ and the moisture variable ϕ is defined at the w points, q_m are defined at the mass points together with the diagnostic variables pressure p and the inverse density α. The grid lengths Δx and Δy are held constant, while the vertical grid length $\Delta\eta$ is not a fixed constant, and decreases monotonically between $\eta = 1$ at the model surface and $\eta = 0$ at the model top.

The waves in the atmosphere have highly variable wavelength, the time step needed to integrate the high-frequency modes are usually much smaller than the time step needed for a stable and accurate integration of the low-frequency modes. To improve

computational efficiency, explicit numerical schemes are used to integrate the high-frequency modes with smaller time steps than what is used on the higher-frequency modes, where longer more economical time steps are used. The method used when splitting the time steps over the different modes is called a time-splitting method. The ARW solver integrates the low-frequency modes using a third-order Runge-Kutta (RK3) time integration sceme, described by Wicker (2002), while the high-frequency are integrated over smaller time steps.

Two time steps are specified when running the ARW model, one for the RK3 scheme and an acoustic time step, for the high-freguency scheme of the time splitting procedure. Both are limited by Courant numbers.

3.1.3 Initial conditions and pre-processing

The ARW solver can calculate idealized flow as well as real-data cases using interpolated data from either an external analysis or forecast. Initial conditions for real-data simulations are pre-processed with the WRF Preprocessing System (WPS) and passed to the real-data pre-processor in the ARW, which generates initial and lateral boundary conditions. The first step WPS does is to define the physical grid, including projection type, location on the globe, number of grid points, nest locations and grid distances. WPS then interpolates to get static fields to the prescribed domain(s). The second step is to process the external analysis or forecast into an internal binary format. WPS interpolates these fields as well onto the projected domain(s).

The input to the ARW real-data processor from WPS contains a 3-dimesional field of the atmosphere at the selected time slices. The 3-dimensional fields contain temperature (K), relative humidity and the horizontal components of momentum data. There are also 2-dimensional time-dependent fields that include surface and sea-level pressure, layers of soil temperature and soil moisture, snow depth, skin temperature, sea surface, temperature and a sea ice flag. The ARW real-data processor then interpolates vertically using functions of dry pressure starting from the top of each column and calculates step-wise down to the surface. The real-data processor also provides ARW with hydrostatically balanced reference state and perturbation fields in addition to metadata specifying date, grid physical characteristics and projection details.

3.1.4 Boundary conditions

The coarsest grid has specified lateral boundary conditions that are supplied by an external file that the real-data processor program generates. The file contains records for the horizontal wind components, potential temperature, humidity and perturbation fields that are used by ARW to constrain the lateral boundaries on all four sides of the coarse domain. The outer rows and columns of the domain are determined by the external file, this edge around the domain is called the specified zone and the width of the edge is typically 1. The next four rows and columns are the relaxation zone, where the model is nudged or relaxed towards the large-scale forecast.

If there are finer domains inside the coarse domain, the ARW supports horizontal nesting. Nesting can either be 1-way or 2-way. The boundary conditions for the finer grid are interpolated by the coarser grid forecast, but for the 2-way nesting the fine grid solution replaces the coarse grid solution for coarse grid points that lie inside the fine grid. The lateral boundary conditions for the nesting behave in the same way as described above, except that the relaxation zone is not active. The prognostic variables are specified in the outer row and column from spatial and temporal interpolation from the coarse grid.

3.2 Model Setup

The Different Simulations

In this thesis there are 3 domains with 27 km, 9 km and 3 km resolution, Figure 3.4 shows the geographical location of the domains. The purpose of this simulation is to simulate the extreme precipitation over Trøndelag from 29 January to 2 February. The model starts 00 UTC 29 January and simulates 120 hours until 00 UTC 3 February. This simulation is called the CRTL simulation. Two additionally simulations with the same domains are run, but with different topography. In the first the topography in Southern Norway is removed to see the effect of the Langfjella mountain ridge. This simulation is called NOTOPO LANG. In the second the topography from Lofoten and southwards is removed, and this simulation is called NOTOPO BIG. Figure 3.5 shows the different topography in the largest 27 km domain for the CTRL, NOTOPO BIG and NOTOPO LANG simulations.

All the 3 simulations are run for the same time period. There are 29 vertical levels and the model has a pressure top of 50 hPa. In adittion there is 1-way nesting between the

coarser and finer domain.

To thest the predictability of the event, 5 simulations with different initial time are started for a large domain with grid spacing of 27 km. The simulation with the earliest initial time starts 00 UTC 25 January, a new simulation starts every 24 h until 00 UTC 29 January. Figure 3.6 shows the domain used for these predictability simulations, the domain covers all of the North Atlantic Ocean and Europe, including eastern parts of Canada and Northwestern Afrika. The domain is sufficiently large so that information updated at the lateral boundaries can not be expected to have substantially influence of the flow over Norway.

Initial and Boundary Conditions

The initial and boundary conditions for all the simulations are analysis from the European Centre for Medium-Range Weather Forecast (ECMWF). The ECMWF analysis have a 0.5 degree horizontal resolution and a temporal resolution of 6 hours.

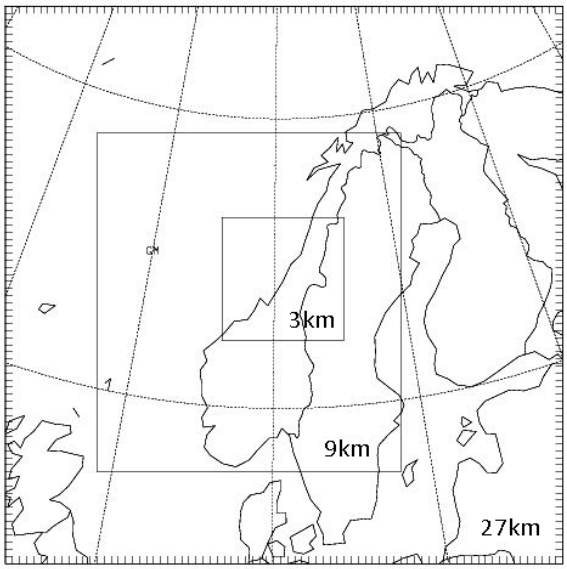

Figure 3.4: The 27, 9 and the 3 km domain.

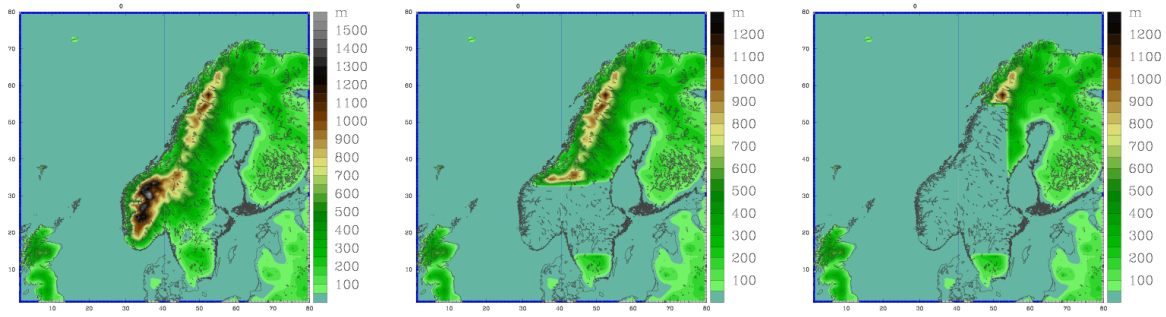

(a) CTRL **(b)** NOTOPO LANG **(c)** NOTOPO BIG

Figure 3.5: Topography for the 3 different simulations.

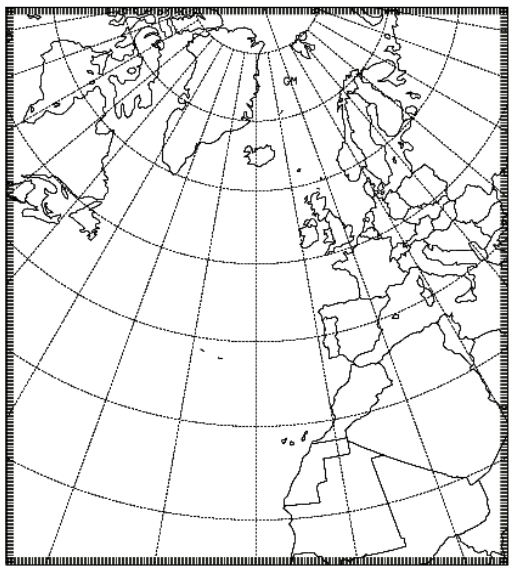

Figure 3.6: Domain with 27 km resolution for the predictability study.

Chapter 4

Data

4.1 Ground observations

The observations from ground stations in this study are collected trough the climate database of the Norwegian Meteorological Institute, eklima.no. Most of the data in eklima.no are from weather stations operated by the Norwegian Meteorological Institute, but some data from other institutions are also made available on this site.

The weather stations can be divided into three different types, manned synoptic stations, automatic stations, and precipitation stations. On the manned stations there are manual observations of cloud cover and cloud characteristics, in addition to automatic measurements of pressure, temperature, humidity, precipitation, precipitation type, and observations of snow cover and depth during winter. Only the latter automatic measurement are done at the automatic stations. Both the manned and the automatic stations send information to the Meteorological Institute 3 - 8 times a day. The precipitation stations provide observations of 24 hour accumulated precipitation at 06 UTC every day. In addition, the precipitation type is observed and during winter, snow cover and snow depth are registered. The precipitation gauges are placed 2 m above the ground.

Observations used in this study is 24 hours accumulated precipitation measured every day at 06 UTC. The temperature, wind speed and wind direction observations used is the mean of measurements taken that day. Table 4.1 shows information about the 14 stations used in the study including the station name, location, meters above sea level, and the station type.

Table 4.1: Stations used in the study.

Name	Latitude	Longitude	m.a.s.l.	Type
Sausvatn - Skogmo	65.30	12.65	55	P
Sula	63.85	8.47	5	M
Halten fyr	64.17	9.41	16	M
Søvatnet	63.23	9.35	306	P
Høylandet - Drangeidet	64.56	12.18	29	M
Leksvik - Myran	63.69	10.61	138	P
Otterøy	64.52	11.29	36	P
Åndalsnes	62.57	7.68	20	P
Trondheim - Voll	63.41	10.45	127	A
Skjækerfossen	63.84	12.02	110	P
Nordøyan fyr	64.80	10.55	33	M
Åfjord - Momyr	64.10	10.53	280	P
Breivoll	63.92	10.42	94	P
Ørland	63.70	9.60	10	M

M - manned synoptic station, A - automatic station, P - precipitation station.

4.2 Gridded precipitation

The gridded precipitation maps used in this study are made by the Norwegian Meteorological Institute for the senorge.no web page[1]. Observed 24 hours accumulated precipitation from approximately 1800 stations in Norway are used to make the map (Mohr, 2008). The observed precipitation data are corrected for measurement losses due to aerodynamical effects near the rim of the gauges, and additional losses due to evaporation and wetting. Each station is assigned an exposure class from 1 - 5, the most sheltered stations are classified as 1 and the most exposed are classified as 5. Most of the stations that are classified as 5 are situated in coastal regions in the western part of the country or high up in the mountains, the extreme sheltered stations are situated in the eastern part of the country.

The spatial interpolation of the precipitation measurements are done by the triangulation method. The triangulation method is fairly quick and creates a set of adjacent, non-overlapping triangles between observational points. One of the advantages of this method is that it requires limited smoothing. The station altitudes are also interpolated by triangulation, using the same triangles as for precipitation. Each point in the 1 km grid is first checked if it lies inside a triangle. A precipitation and altitude value is then linearly interpolated to the point by using vectors from each triangle corner.

[1]The senorge.no webpage is a collaboration between the Norwegian Meteorology Institute, the Norwegian Water and Energy Directorate (NVE), and the Norwegian Mapping Authorities (SK). It contains daily and monthly annual snow, temperature, precipitation and water maps over Norway.

The last step in making the map is to correct the gridded precipitation for altitude height. The interpolated altitude map is used in combination with a digital elevation model of Norway. Under 1000 m the precipitation is expected to increase by 10 % for each 100 m increase in altitude. Over 1000 m there is only a 5 % increase for each 100 m.

4.3 Satellite data

The satellite data used in the study are from the Hamburg Ocean Atmosphere Parameters and Fluxes from Satellite Data (HOAPS)[2] archive. The data set is satellite based climatology of precipitation, turbulent heat fluxes and freshwater budget in addition to other related atmospheric state variables over the global ice free oceans. The variable used in this study is precipitation derived from the Special Sensor Microwave/Imager (SSM/I) passive microwave radiometers.

The data set provides data twice daily with 1 degree resolution and globally gridded. Every grid cell contains only one satellite overpass, early overpasses are overwritten by later overpasses. This method provides a more spatial homogeneity than averaging all the available data. Each grid cell contains the satellite overpass closest to 12 and 24 UTC respectively (Andersson *et al.*, 2007).

4.3.1 SSM/I

A SSM/I is a scanning radiometer, and operates on the four frequencies 19.35, 22.235, 37, and 85.5 GHz. Their orbit is near-circular, sun-synchronous, and near-polar with an inclination of 98.8°. The period of the orbit is 102 minutes and has an nominal altitude of 860 km, with a variance of 25 km due to eccentricity and the oblateness of the Earth.

Figure 4.1(a) shows the satellite geometry. The SSM/I rotates continuously about the vertical axis parallel to the local spacecraft. When looking towards the tail of the spacecraft, the scan direction is from the left to the right with an angle of ± 51.2°. The resulting active scan angle is 102.4°, and a swath width of 1400 km (Hollinger *et al.*, 1990). Figure 4.1(b) shows the satellite observation coverage over 24 hours. The satellite has done a complete coverage of the Earth in two to three days, except for two small circular sectors at 2.4°centered on the North and South poles. The

[2] hoaps.org

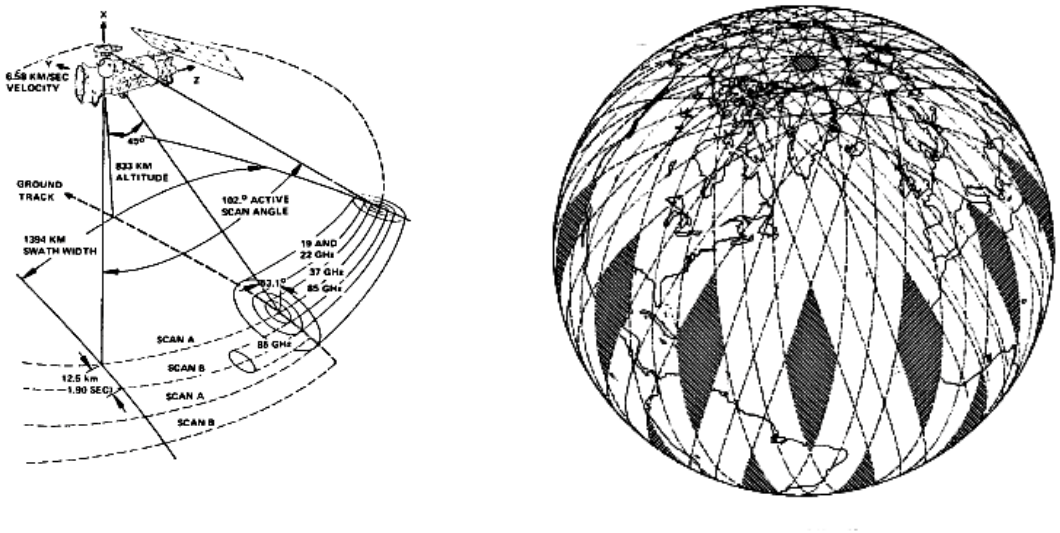

(a) **(b)**

Figure 4.1: (a) The satellite geometry. (b) Earth coverage for a 24 hour period, only the shaded regions are not covered during this time period, both from Hollinger *et al.* (1990).

SSM/Is are carried onboard the Defense Meteorological Satellite Program (DMSP) polar orbiters.

4.3.2 Retrieving precipitation rates.

An algorithm based on the fundamental principles of radiative transfer is used to find the rain rate R over the oceans. The all-weather algorithm is an integration of the non-rain algorithm in Wentz (1997), where the near-surface wind speed W, columnar water vapor V, and the columnar cloud liquid water L, is found with the observed brightness temperature T_B. The all-weather algorithm also includes a rain algorithm, where the effective radiating temperature T_U is included (Wentz & Spencer, 1996).

The first step of retrieving precipitation rates is to calculate the atmospheric transmittance of liquid water τ_L in addition to the parameters W, V, and T_U. The parameters are found by varying their different values until they match the observed T_B. If there is rainfall, τ_L is related to the columnar water in the rain cloud. For retrieving τ_L, it has to be possible to separate the τ_L signal from the T_U signal in the observed T_B polarization signature. Because the rain field is not uniform, different corrections has to be done before the mean atmospheric attenuation for liquid water A_L is found. To convert the A_L to columnar rain rate, the Mie scattering theory and an assumed relationship between cloud water and rain water are used. The final step for finding precipitation rate is to convert the columnar rain rate by dividing it with an assumed rain column

height which is a sea surface temperature climatology function. The algorithm found here are are part of the NASA pathfinder program.

4.4 HYSPLIT trajectory model

Trajectories used to find the origin of the air masses in this study are calculated with the HYSPLIT model (Rolph, 2010; Draxler & Rolph, 2010). HYSPLIT stands for HYbrid Single - Particle Lagrangian Integrated Trajectory. It is designed for quick response to atmospheric emergencies, diagnostic case studies or climatological analysis using previously gridded meteorological data. The model can both be run interactively on the READY website, and it can be installed on a PC.

The atmospheric data used for the computations are output fields from numerical models. Usually some pre-prossesing is needed before the data can be used by the HYSPLIT model. The vertical coordinate system in the output file are linearly interpolated to a terrain - following (σ) coordinate system.

$$\sigma = 1 - \frac{Z_{top} - Z_{mslp}}{Z_{top} - Z_{gl}} \tag{4.1}$$

All the heights are expressed relative to terrain and where Z_{top} is the top of the HYSPLIT coordinate system. The horizontal coordinate grid system is kept the same as in the output file. The model needs as a minimum the horizontal wind coordinates, temperature, height or pressure, and the surface pressure. If there is no vertical wind component in the data file, or other restrictions are set on this variable, the HYSPLIT model can compute this missing field.

When the basic meteorological data (U, V, W) are processed and interpolated to the vertical model grid, the trajectories can be computed. The new position is calculated from the average wind velocity at the initial position P, and the first-guess position P'. Equation 4.2 shows how the first-guess position is computed. The time step is variable, but with the restriction $V_{max}\Delta t < 0.75$.

$$P'(t + \Delta t) = P(t) + V(P(t))\Delta t \tag{4.2}$$

$$P(t + \Delta t) = P(t) + \frac{V(P(t) + V(P'(t + \Delta t))}{2}\Delta t \tag{4.3}$$

The meteorological model used in this study is Reanalysis data from NCEP/NOAA. The vertical motion calculations are used from the model owns vertical velocity.

Chapter 5

Synoptic Situation

5.1 Circulation 500 hPa

On 28 January a high-pressure is established over the British Isles. Together with a low-pressure to the south of Greenland, and another low-pressure over Russia, the high-pressure forms an omega shape pattern in the geopotential height surfaces. This type of pattern in the geopotential height surfaces can be characterized as an omega blocking event. A blocking event can be defined as a state where the circulation in the normal westerly zonal flow is interrupted in one or more sectors by a strong, persistent, meridional-type flow (Elliott & Smith, 1949). The surface system in a blocked sector is usually comprised of a warm anticyclone in high latitudes and a cold depression in lower latitudes upstream and/or another cold depression downstream of the high. If there occurs an intensification of the flow, the high-pressure has a tendency to move westward. During flow dissipation, the high pressure has a tendency to move eastward (Sumner, 1954). Blocking events are most frequently on the northern hemisphere during winter and spring.

The high-pressure is most intense on the three days from 29 January to 31 January. There is a strong geopotential gradient around the norther side of the high-pressure. This gradient extends from the North-Atlantic at roughly 40°north and 40°west, across Iceland, Central Scandinavia and into Russia, see Figure 5.1(a). Over Norway the geopotential gradient from the southern to northern part is 650 m on 29 January, and 600 m on 30 January and 31 January. On the following two days the high-pressure gets weaker, and the omega shape is disrupted, this is also visible in the anomaly heights. On 1 February and 2 Febraury, the high-pressure anomaly has moved westward and is situated on the east side of Iceland. Figure 5.1 shows the geopotential height (b)

and the geopotential height anomaly (d) at 500 hPa on 1 February. At the end of the period the omega shape is almost diminished and a more zonal flow is established. The low-pressure south of Greenland has also moved east, however the low-pressure over Russia has stayed stable during the entire period.

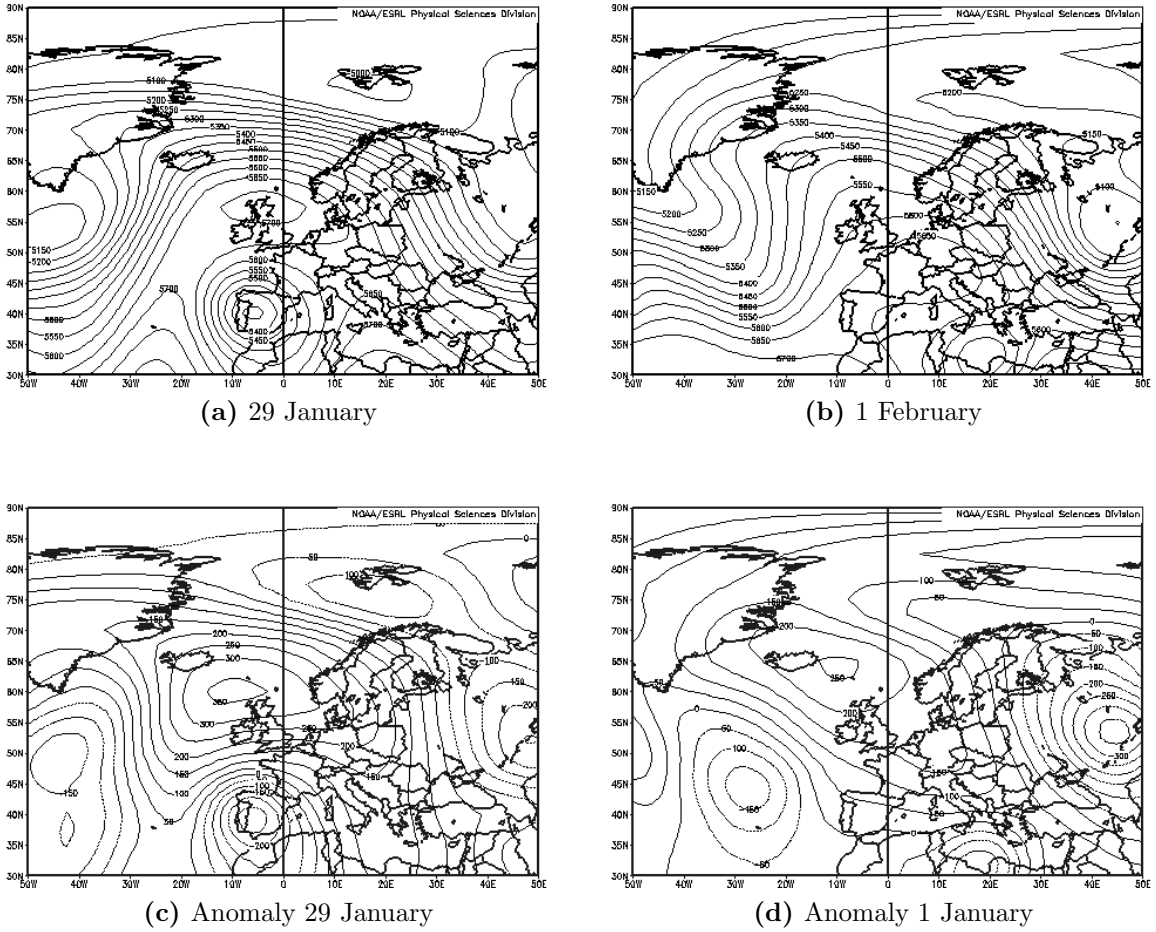

(a) 29 January **(b)** 1 February

(c) Anomaly 29 January **(d)** Anomaly 1 January

Figure 5.1: The geopotential height [m] at 500 hPa for 30 January (a) and 1 February (b), the geopotential height anomaly [m] from the climatology mean (1968-1996) at 500 hPa for the same days (c) and (d). 50 m interval. Data from NCEP/NCAR, acquired through NOAA/CDC.

5.2 Temperature anomaly

Due to the strong meridional flow described above, warm air is transported northwards. During the six day long period, a positive temperature anomaly was present over the North Atlantic Ocean, the Norwegian Sea and Scandinavia at 500 hPa. The anomaly was strongest on 30 January, Figure 5.2(a) shows a positive anomaly of 12 K over the Norwegian Sea at 500 hPa. Over Central Norway the temperature anomaly is 10 K. There is a strong negative anomaly over Gibraltar and the surrounding areas. At

the end of the period the positive temperature anomaly over Scandinavia weakens and moves west.

Figure 5.2(b) shows the temperature anomaly at 850 hPa on 30 January. The largest positive temperature anomaly at this pressure level is 10 K over the Skagerrak strait. The lower temperature anomaly at lower pressure levels can indicate a statically stable atmosphere. Most parts of Northern Europe experienced higher temperatures than average, but there are two negative anomalies south of Greenland, and over Russia and Ukraine. These two negative anomalies corresponds to the two low pressures.

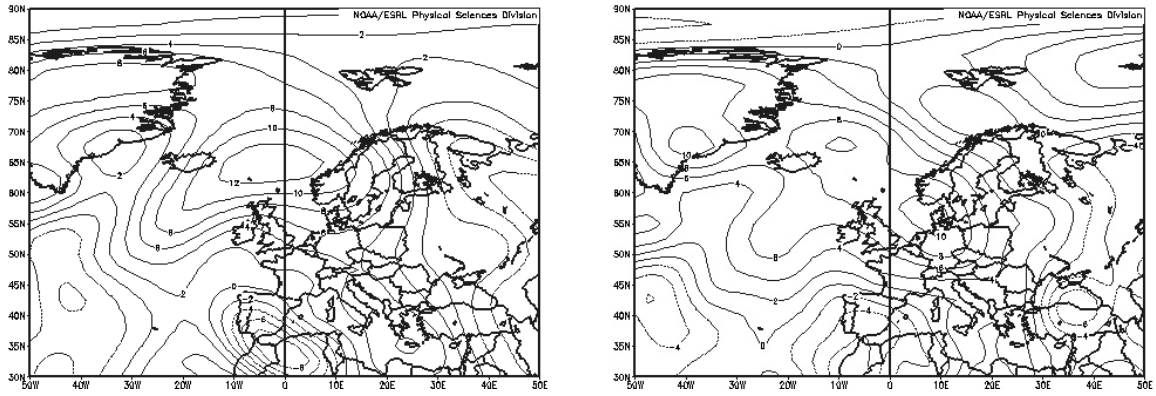

(a) 500 hPa **(b)** 850 hPa

Figure 5.2: Temperature anomaly from the climatology mean (1968-1996) at 500 hPa (a) and 850 hPa (b), 2°K interval. Data from NCEP/NCAR, acquired through NOAA/CDC.

5.3 Surface analysis

The high-pressure over the British Isles is also the dominating factor in the surface circulation. The position of the high-pressure at sea level is almost identical to the position of the high-pressure aloft, this leads to limited vorticity advection and a very stationary situation. The pressure is highest at the beginning of the period, where the pressure center is over 1035 hPa. Figure 5.3(a) shows the surface analysis at 12 UTC on 29 January, there are a strong gradient in the pressure surfaces over Central Norway and there is reported an overcast sky at the synoptic station on the Fosen peninsula, Ørlandet. To the north of the high-pressure fronts pass over the Northern Norway. The pressure surfaces over Central Norway converges, and stronger more southerly winds are measured at Ørlandet, see Figure 5.3(b). Towards the end of the period, the high-pressure weakens and moves east.

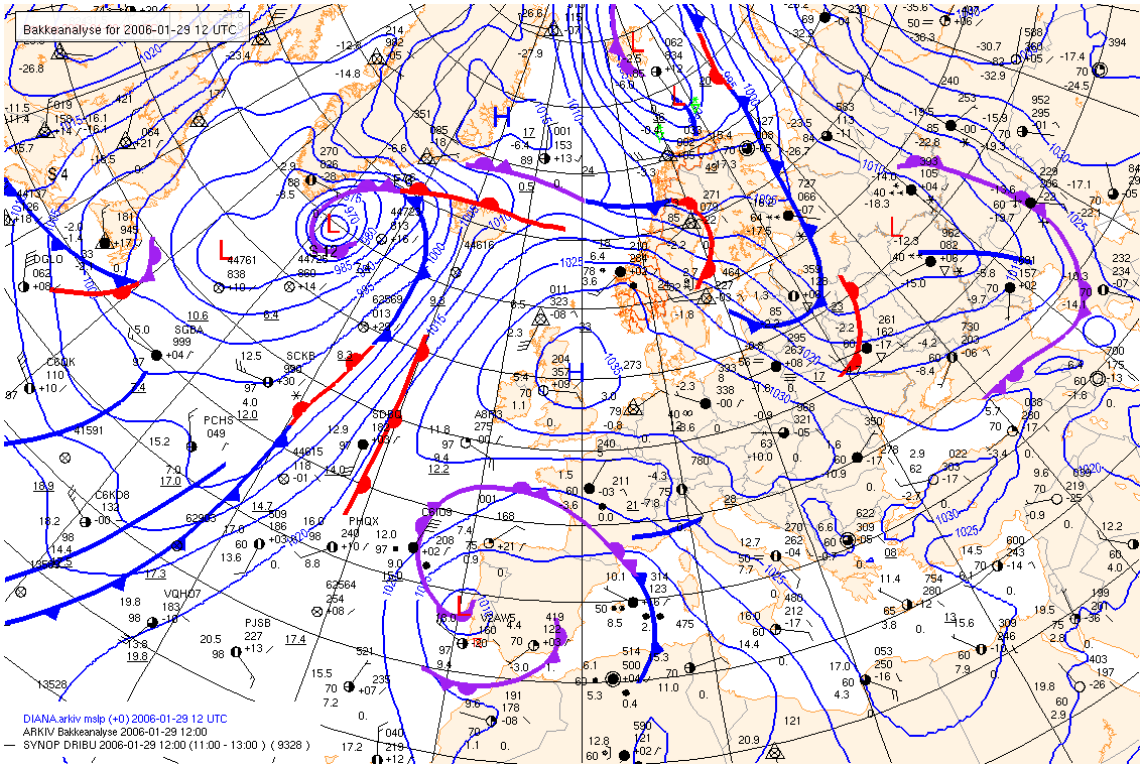

(a) 29 January 12 UTC

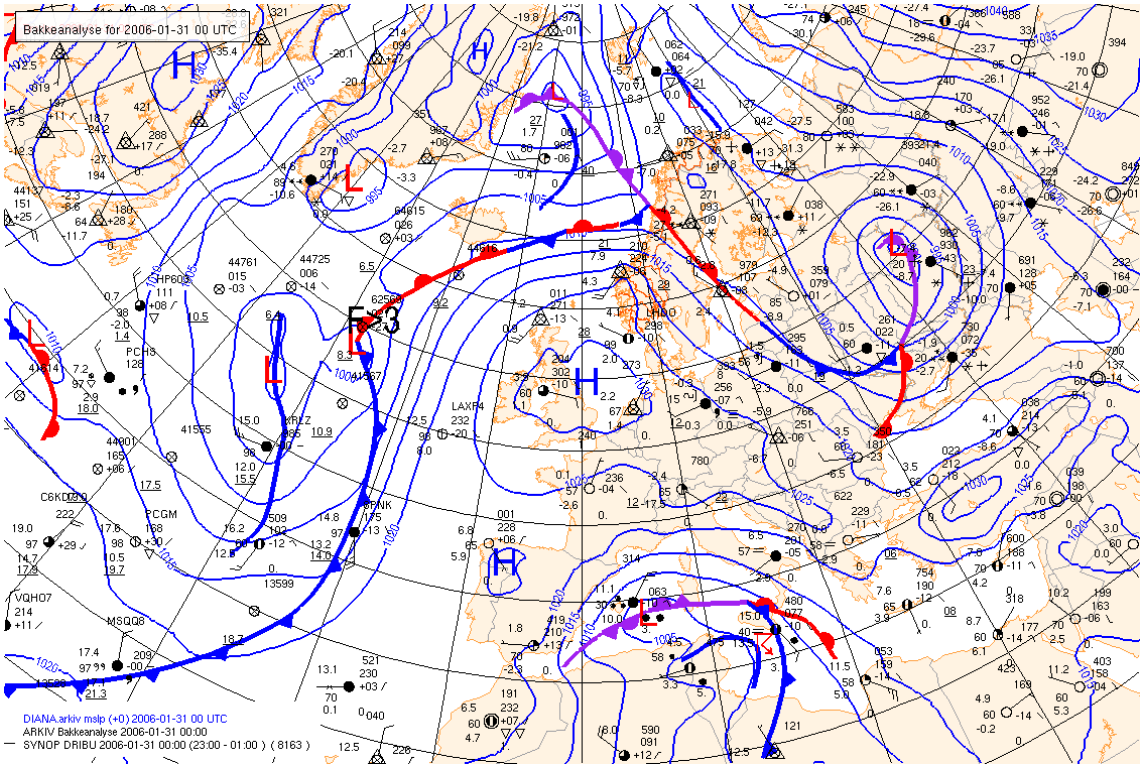

(b) 31 January 00 UTC

Figure 5.3: Surface analysis and observations from the Norwegian Meteorological Institution, at 12 UTC 29 January (a) and 00 UTC 31 January (b). 5 hPa interval.

5.4 Precipitation

Strong persistent westerly winds together with warm temperatures cause heavy precipitation over Central Norway during the event. At the beginning of the period, the precipitation field is dispersed over Central Norway and northwards. The highest 24 hours accumulated precipitation was measured at 06 UTC 31 January. Figure 5.4 shows interpolated 24 hours accumulated precipitation from observation at 06 UTC 31 January, method for making the map is described in chapter 4.2. The station with the highest measured precipitation is Åfjord-Momyr with 143.9 mm/24h on 31 January and 113.5 mm/24h on 1 February. The precipitation normal for this station is 175 for January and 147 mm for February. This means that around 80 % of the precipitation expected to come during the two months came in two days. Several other stations had record high measurements on 31 January. Otterøy measured 101.5 mm/24h on 31 January, and the January normal at this station is 141 mm. Halten fyr measured 54.5 mm/24h on 31 January, and the January normal is 79 mm.

The precipitation field in the figure is more intensified on 31 January over Central Norway than for the two previous days. A peninsula on the coast of Central Norway called Fosen receives the most precipitation with around 150 mm/24h, the mountains in this peninsula reach up to 700 meters above sea level. There are two other areas that receives over 100 mm/24h to the north and east of the peninsula. Towards the end of the period, the precipitation field moves even further south and there are measured less precipitation. During the whole period, the Fosen peninsula received up to 500 mm in some areas, this is that same amount that some stations receive during the whole year in the inland of Southeastern Norway.

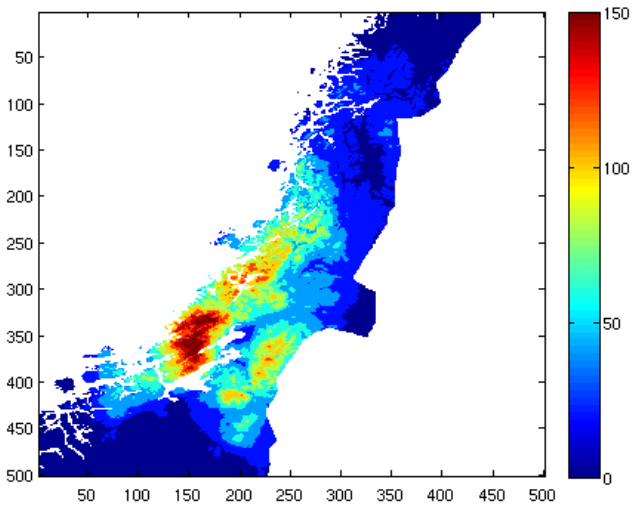

Figure 5.4: Precipitation map over Central Norway 24 hours accumulated precipitation at 06 UTC 31 January, (Mohr, 2008)

Chapter 6

Climate

It is important to study the effects global climate change may have on the frequency of the same kind of extreme precipitation events that are studied in this thesis. Climate change is expected to affect the frequency of extreme weather, mostly due to higher temperatures and the intensification of the hydrological cycle. From the previous chapters, four atmospheric parameters are found important for such events to occur. The first parameter is heavy precipitation, which is rather self-explanatory, but there can be substantial errors in this factor due to unresolved topography in the coarse climate model and uncertainties in the parameterization of precipitation processes. High wind speeds and westerly wind directions are important for the topographic lifting of the impinging flow when reaching the mountains of Central Norway. Temperatures are important for the right type of precipitation and snow-melting during winter. It is also important that the higher temperature an air parcel has the more moisture the parcel can contain.

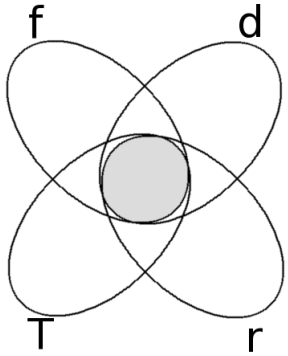

Figure 6.1: Important atmospheric parameters for creating a similar extreme precipitation event, wind speed (f), wind direction (d), precipitation (r) and temperature (T).

Figure 6.1 shows schematically the four important parameters. From the observations there are defined thresholds for each factor, all of the thresholds have to be exceeded

for a similar event to be expected (the grey shaded region).

6.1 Observations

Observations from the weather station at Ørlandet are used to analyze the frequency of similar events in present climate. The measurement series are mean daily temperature, mean daily wind speed and wind direction, and 24 hours accumulated precipitation measured at 06 UTC every day. The series are from 1 January 1957 to 31 December 2008. The daily mean temperature measured on 30 January 2006 at Ørlandet was 6.7°C, and the mean wind speed was 15.4 m/s. On January 31, the mean temperature was 7.4°C, and the mean wind speed was 14.9 m/s. On both days the mean measured wind direction was close to 250°. The 24 hours accumulated precipitation is measured at 06 UTC every day, most of this precipitation therefore represent what fell on the previous day. The measurement taken the next day will be used to represent the precipitation of the studied days. The precipitation measured at 06 UTC 31 January was 42.7 mm/24h, only seven times has there been observed higher amounts of precipitation at this station during the 52 year long measurement series. On the next day, 1 February the precipitation measured was 17.2 mm/24h.

The threshold values for events of this kind are chosen based on the observations described above, but rounded down for temperature, precipitation and wind speed, and a relatively wide sector of westerly winds is defined. The temperature threshold is set to 6.5 °C, the wind speed to 12 m/s, and the precipitation to 20 mm/24h. The wind direction are set from sectors 195°to 345°. Table 6.1 shows the probability for a measurement to fulfill one criteria, and the probability to fulfill all four. This is done for both measurements taken during the whole year, and measurements taken from November to April. The wintertime data are important for the evaluation of the probability for 'complex extremes', events where snow-melting in addition to high precipitation lead to increased flooding.

During winter there is a higher probability of stronger winds, but a lower probability for westerly winds. Figure 6.2 shows the distribution of the temperature, wind speed, precipitation and wind direction measurements at Ørlandet station with the probability on the y-axis. Measurements over the blue shaded region is over the thresholds, or inside the westerly wind direction sector. The temperature threshold is near the center of the temperature distribution for measurements taken during the whole year, while during winter most of the temperature measurements are below the threshold. This factor is also most important during winter.

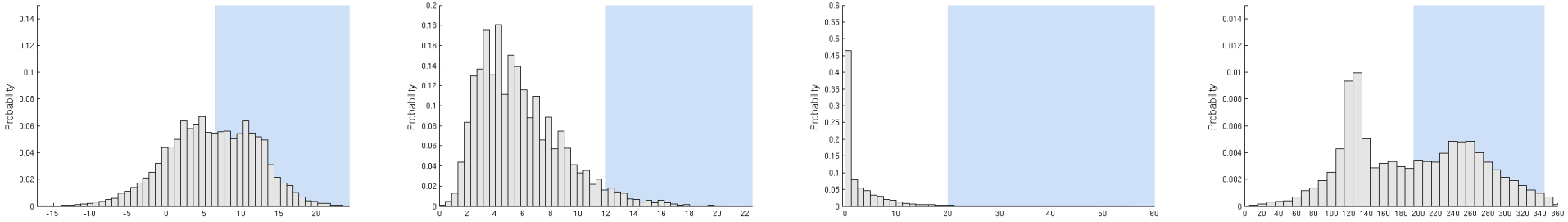

(a) Temperature whole year (°C)

(b) Wind speed whole year (m/s)

(c) Precipitation whole year (mm/24h)

(d) Wind direction whole year (°degree)

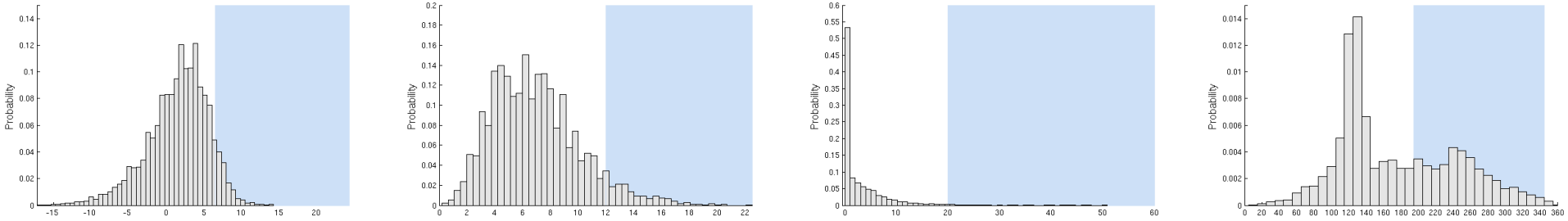

(e) Temperature winter (°C)

(f) Wind speed winter (m/s)

(g) Precipitation winter (mm/24h)

(h) Wind direction winter (°degree)

Figure 6.2: Distribution of the different atmospheric parameters from the measurement series from Ørlandet for the whole year (a)-(d), and for the wintertime measurement from November to April (e)-(h) with the probability on the y-axis. The blue shaded regions show the observation over the threshold values, or inside the westerly wind direction sector given in Table 6.1.

Table 6.1: Probability to fulfill criterial for observations.

Whole year			Winter (Nov-Apr)		
Threshold	Probability of		Threshold	Probability of	
	one	all four		one	all four
T $\geq$ 6.5 ° C	47.9 %	0.46 %	T $\geq$ 6.5 ° C	8.5 %	0.36 %
f $\geq$ 12 m/s	4.3 %		f $\geq$ 12 m/s	7.1 %	
r $\geq$ 20 mm/24h	1.4 %		r $\geq$ 20 mm/24h	1.2 %	
195° $\leq$ d $\leq$ 345°	46.3 %		195° $\leq$ d $\leq$ 345°	36.0 %	

The probability of a measurement to be over the three thresholds for the whole year and for the winter months, and to be from a westerly wind direction. The probability for the mean daily values to fulfill all four criteria are also shown.

6.2 Climate model simulations

The probability of an increase in frequency of similar events due to climate change is explored by studying data from a climate model forced by a future greenhouse gas scenario. Downscaling General Circulation Models (GCMs) with Regional Climate Models (RCMs) is done to investigate the regional effects of global climate change and to reduce the uncertainties that a coarse model has over areas like the Alps, the Mediterranean, or Scandinavia, where coarse resolution is unable to resolve the large spatial variability. The simulated climate data is made available trough the ENSAMBLES project[1]. This project is a continuation of the PRUDENCE project[2], which goal was to downscale the coarse GCMs.

The ECHAM5 model is used for the large scale simulation of the control period from 1971-2000, and for the future projection with the A1B greenhouse gas scenario from 2071-2099. The A1B scenario describes a future world of very rapid economic growth during the 21st century, a global population peak at mid-century succeeded by a declination, rapid introduction of new and more efficient technology, in addition to a balance between energy sources. The ECHAM model is developed from the ECMWF operational forecast model (therefore the two first letters EC), and a comprehensive parameterization package developed at the Max Planck Institute for Meteorology (MPIM) in Hamburg (hence the 3 last letters HAM) (Roeckner *et al.*, 2003). The GCM is downscaled with the HIRLAM regional climate model (Christensenm *et al.*, 1996) with a horizontal resolution of 25 km. The simulated data series represent values at Ørlandet.

[1]http://ensembles-eu.metoffice.com
[2]http://prudence.dmi.dk

Control simulation

In order to study the probability of similar extreme events in the climate model future scenario, the models capability to recreate the real world needs to be studied with the use of a control simulation. New threshold values also need to be set for the modeled data. In this study, these values are defined in view of the probability of observed temperature, wind speed and precipitation at Ørlandet station in the present case, see Table 6.1. When defining threshold values or percentiles for the climate simulations, the temperature threshold is rounded to 45 %, wind speed is rounded up to 10 % and precipitation is rounded up to 5 %. The thresholds found from the probabilities in the control simulation for the whole year are used as thresholds for the winter time data as well. All westerly winds are included from 180°to 360°.

Table 6.2: Probability to fulfill criterial for the control simulation.

	Whole year		Winter (Nov-Apr)	
Parameter	Probability of		Probability of	
	one	all four	one	all four
T	45.0 %	0.72 %	6.0 %	0.28 %
f	10 %		14.8 %	
r	5 %		3.7 %	
d	30.2 %		23.8 %	

The probability for the control simulation to exceed the temperature, wind speed and precipitation thresholds, and the probability of westerly winds in the whole year and winter time data. The probability to fulfill all four criterial is also shown.

Table 6.2 shows the probability for the control simulation data to exceed the thresholds, and for a westerly wind direction. The probabilities to fulfill all four criteria for the whole year and winter time data is also shown. The simulated data has a smaller probability for westerly wind directions than what is observed. Figure 6.3 shows the wind roses for the observed data for the whole year (a) and for the winter time (b). (c) and (d) show the same for the climate model control simulation. The observed wind roses show high frequencies for winds from southeast, the highest frequency of winds from this direction is during winter with roughly 14 %. The roses also shows higher frequencies for winds from southwest to west, these directions have the highest frequencies in the rose for the whole year with around 5 %. There are only few observations of winds from a northerly direction. The roses from the control simulations also show a maximum frequency if southeasterly winds, but they are distributed over a wider sector than the observations. The westerly and northerly winds are not represented well in the model, especially during the winter months. The model also overestimates the wind speeds compared to measured values. The temperatures from the model control simulation follow the same distributions as the observed, but the modeled do not recreate the extreme warm or cold temperatures. The precipitation data are also well

modeled (not shown).

Future projection

The same thresholds that are defined for the control simulation are also used for the future projection simulation.

Table 6.3: Probability to fulfill criterial for the future projection.

Parameter	Whole year		Winter (Nov-Apr)	
	Probability of		Probability of	
	one % *increase*	all four % *increase*	one % *increase*	all four % *increase*
T	59.5 % *32.3* %	1.19 % *65.28* %	22.6 % *278.6* %	0.65 % *132.14* %
f	9.7 % *-2.9* %		13.8 % *-6.2* %	
r	6.8 % *35* %		3.7 % *-0.3* %	
d	30.2 % *5.6* %		23.8 % -6.8 %	

The probability for the future projection to exceed the temperature, wind speed and precipitation thresholds, and the probability of westerly winds for the whole year and winter time data. The probability to fulfill all four criterial is shown. The percent increase from the control run to the future projection are shown in italic.

Table 6.3 shows the probability for the future projection data to fulfill each of the criteria, and the probability to fulfill all four for the whole year and wintertime. The percent increase from the control simulation to the future projection are also calculated and shown in italic. Number of warm events in the winter has the highest increase (278.6 %). Looking at the whole year, there is a 32.3 % increase in the number of events that exceed the temperature threshold, and 35 % increase in the number of events that exceed the precipitation threshold. The number of heavy precipitation events increases more in the summer than in the winter, as can be seen when comparing the data for the winter and the whole year. Figure 6.3 shows the wind roses for the control simulation and the future projection for the whole year and winter time data ((c) to (f)). The future projection wind rose is quite similar to the wind rose in the control simulation. The Table 6.3 also show minor differences in the wind data.

There is calculated a 65.28 % increase in events where similar extreme precipitation events can be expected for the whole year. All the factors show an increase except for the wind speed. For the wintertime data a fairly high increase of 132.14 % is found, yet only the temperature factor increases during these months.

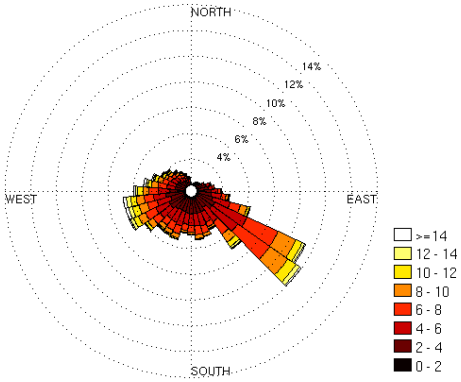

(a) Measured whole year

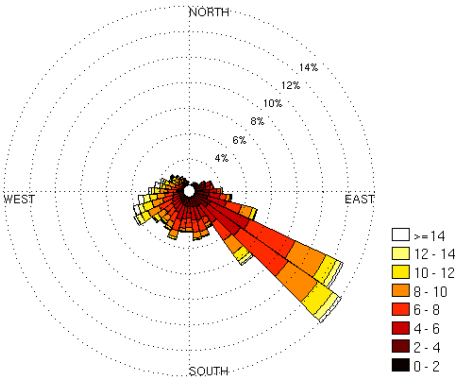

(b) Measured winter

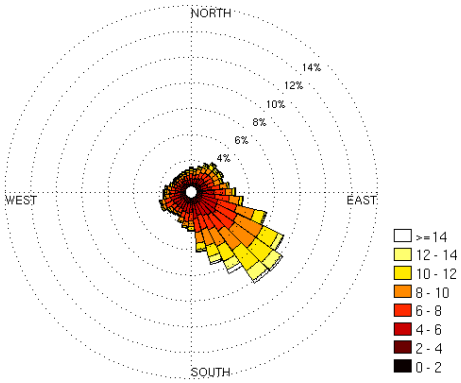

(c) Control simulation whole year

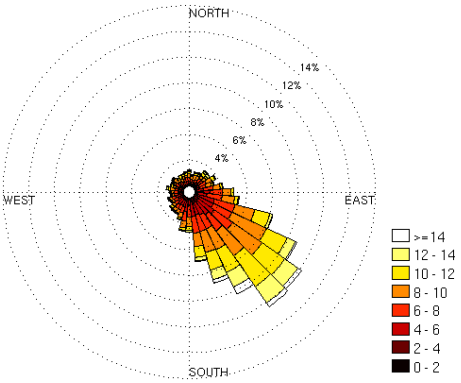

(d) Control simulation winter

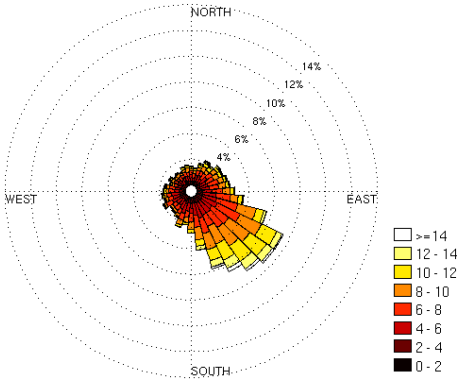

(e) Future scenario whole year

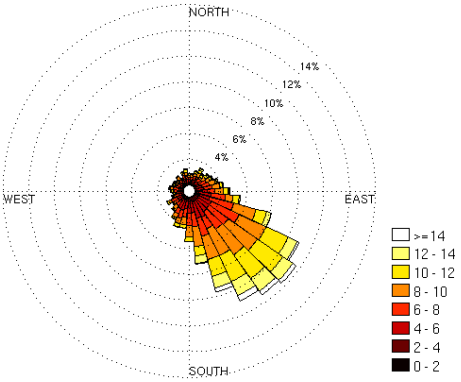

(f) Future scenario winter

Figure 6.3: Wind roses for observed winds at Ørlandet for the whole year (a) and the winter (Nov-Apr) (b), for the simulated control simulation for the whole year (c) and the winter (Nov-Apr) (d), and for the future scenario simulation for the whole year (e) and the winter (Nov-Apr) (f). The numbers on the right side of each rose indicate wind speed m/s.

6.3 Discussion

One important result found in the future projection data is the increase in the frequency where temperatures are over the threshold. This increase is highest for the wintertime data. Increased wintertime temperatures have also been found in several other studies on climate change over Scandinavia (e.g. Hanssen-Bauer *et al.* (2005); Haugen & Iversen (2008); Beldring *et al.* (2008)). Combined events of high temperatures and high precipitation are studied by Benestad & Haugen (2007), and finds an expected increase in frequency. Another result from the future projection data is the increase in frequency of precipitation events over the threshold. This increase is however only present in the summer months.

Apart from the study by Benestad & Haugen (2007), there is no other studies that focuses on events where two or more factors are combined in studies of the frequency change in extreme weather events over Norway due to the global climate change. It is important to study such combined events because the increase or decrease in one parameter can show another tendency when combined with another parameter. In this study there is found an increase in extreme precipitation events from the wintertime climate data. However for the wintertime data, the only factor that shows an increase the probability to exceed the temperature threshold. The precipitation has a small decrease during winter. This effect is not visible when studying the sole precipitation parameter.

There is found a shortcoming in the model when recreating the observed wind speeds and directions. A better modeling of the frequency of westerly wind directions may provide a higher positive response for extreme precipitation events in the future projection.

Chapter 7

PAPER

Extreme Precipitation in Central Norway

Birthe Marie Steensen[1], Haraldur Ólafsson[1,2,3], and Marius O. Jonassen[1]

[1]*Bergen School of Meteorology, Geophysical Institute, University of Bergen*
[2]*University of Iceland*
[3]*Icelandic Meteorological Office*

Abstract

At the end of January and beginning of February 2006, an extreme precipitation event occurred over Central Norway. The precipitation in addition to warm temperatures produced flooding and landslides that caused damage to infrastructure. The event is explored with conventional data, data from remote sensing and numerical simulations. It is shown that there is very little quasi-geostrophic forcing and that the extreme precipitation is locally generated by strong and persistent winds impinging the mountains. The mountains in SW-Norway, far away from the precipitation, contribute significantly to the extreme, by blocking, deflection and enhancement of the low level flow. The warm and humid airmass involved is shown to originate in the sub-tropics. Assessment of forecasts with different lead times reveal a sensitivity to a baroclinic system to the east of Newfoundland three days prior to the event in Central Norway.

1 Introduction

At the end of January and beginning of February 2006, and extreme precipitation event occurred in Central Norway. The precipitation occurred together with high temperatures and snow melting that lead to severe flooding, damage of infrastructure, and loss of human life. In spite of the severity of this kind of events and the importance of forecasting them accurately, they have not been described in detail in the scientific literature and the capability of the current state-of-the-art numerical models to reproduce such events is not clear.

A sole study, to the knowledge of the authors of this paper, describes an event of a similar kind, but with a primary emphasis on the origin of the airmasses arriving from low latitudes and the large scale circulation (Stohl *et al.* , 2008). In a climate change context, there are more studies of extreme precipitation in this region of the world: In a study of spring-time precipitation and high temperatures, Benestad & Haugen (2007) concludes that high-rainfall-high-temperature events can become more frequent and produce a greater risk of spring time flooding in a future climate. In fact, downscaling of global climate simulations with regional climate models indicate higher rainfall intensity and warmer temperature in Western Norway in the future (Hanssen-Bauer *et al.* , 2003; Haugen & Iversen, 2008; Beldring *et al.* , 2008).

In this paper, the 2006 wintertime extreme precipitation event over Central Norway is studied. The Meso- to synoptic scale flow pattern associated with the event is described and the ability of a numerical tool to reproduce the extreme precipitation is evaluated with the help of measurements from a network of precipitation observations collected trough the Norwegian Meteorological Institute climate database (eklima.no) and satellite observations. The roles of synoptic-scale forcing and topographic enhancement are established. The airmass is traced and forecasts from different initial conditions are evaluated.

The second section of this paper gives a short description of the synoptic situation during the event, the third section is a short description of the model used for the simulations. The results are presented in the fourth section, followed by a discussion, summary and conclusions.

2 The Synoptic Situation

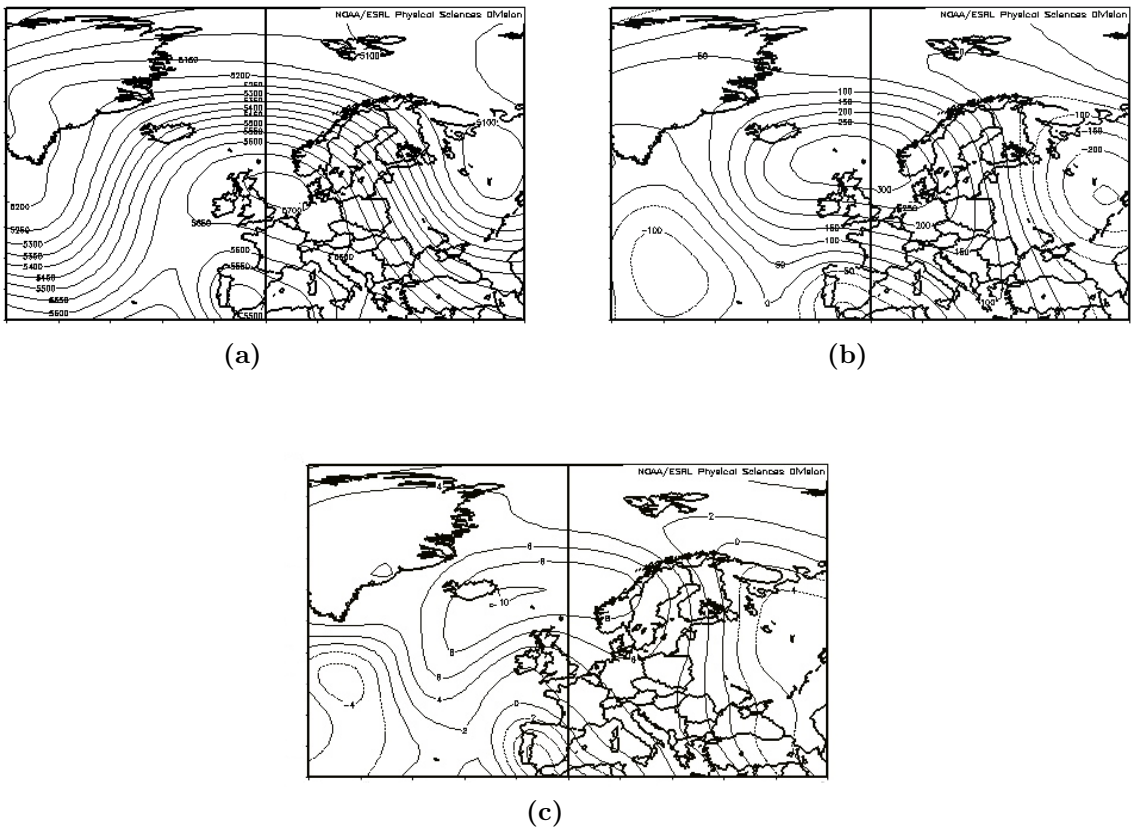

Figure 1: Synoptic plots for 29 to 31 January 2006 (a) mean geopotential height [m] at 500 hPa with intervals of 50 m. (b) mean geopotential height anomaly from the Climatology mean (1968-1996) at 500 hPa with intervals of 50 m. (c) temperature anomaly at 500 hPa (intervals of 2 K). Data from NCEP/NCAR, acquired through NOAA/CDC.

The synoptic situation during the event was characterized by a high-pressure over Great Britain with low-pressure systems to the west and east of it. Figure 1(a) shows the mean geopotential height in 500 hPa over 3 days from 29 to 31 January 2006. There

is a distinguished omega shape pattern in the flow. The areas affected by blocking can experience the same kind of weather for an extended period of time and this was indeed the the case during the presently discussed event. Figure 1(b) shows the anomaly of the geopotential height at 500 hPa over the same period, the geopotential height over Great Britain is more than 300 m higher than the average. The two lows, one south of Greenland and the other one over Russia are also shown. Figure 1(c) shows the temperature anomaly at 500 hPa. Over Norway, the temperature is 6-8 K above average. The maximum positive anomaly of 10 K is located southeast of Iceland, while in Southern Europe the temperatures are lower than average.

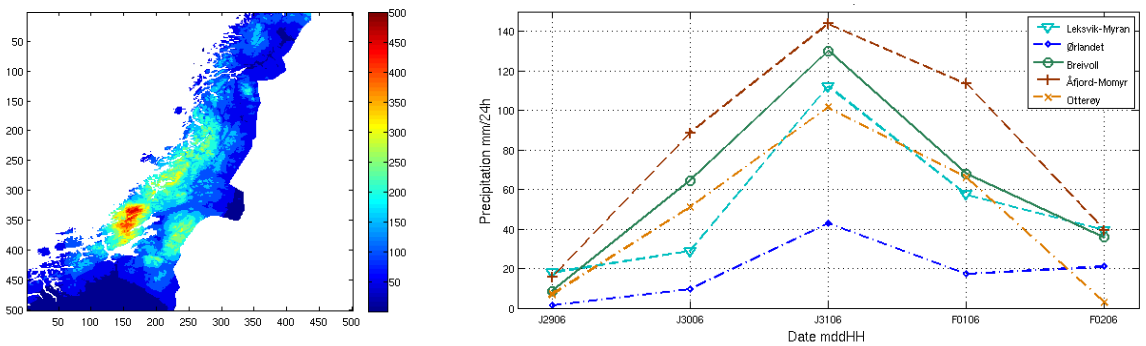

(a) **(b)**

Figure 2: (a) Interpolated measured 120 hours accumulated precipitation with 1 km resolution (Mohr, 2008) from 06 UTC 29 January to 06 UTC 2 February. (b) Graphs showing accumulated precipitation (mm/24h) measured at 06 UTC from 5 stations from 29 January to 2 February.

Central Norway experiences heavy precipitation for several days. Figure 2(a) shows the observed accumulated precipitation for five days from 06 UTC 29 January to 06 UTC 02 February. The measurements are corrected for losses due to aerodynamical effects, adjusted for height differences between station point and grid point, and interpolated to a 1 km grid, for more information see Mohr (2008). Figure 2(b) shows 24 hour accumulated precipitation measurement series over the same 5 days from the four stations that had the highest measured precipitation in addition to measurement taken at the Ørlandet station for observations taken 06 UTC every day. The highest 24 hour accumulated precipitation measured are from the observations at 06 UTC on 31 January. Åfjord-Momyr had the highest measured precipitation of all the stations with 143.9 mm/24h 06 UTC 31 January and 113.5 mm/24h 06 UTC 1 February. All the stations are situated on the Fosen peninsula except for Otterøy, which is situated just north of it. This is in agreement with Figure (a) that also shows most precipitation in the peninsula and in surrounding areas. Figure 3 shows where the stations are situated and other locations that are mentioned in the text.

3 The Numerical Simulations

The period was simulated using the Weather Research and Forecasting (WRF) Model, version 3.0.1. The Advanced Research WRF (ARW) solver integrates the compressible, nonhydrostatic Euler equations. For more details about the model see Skamarock (2008).

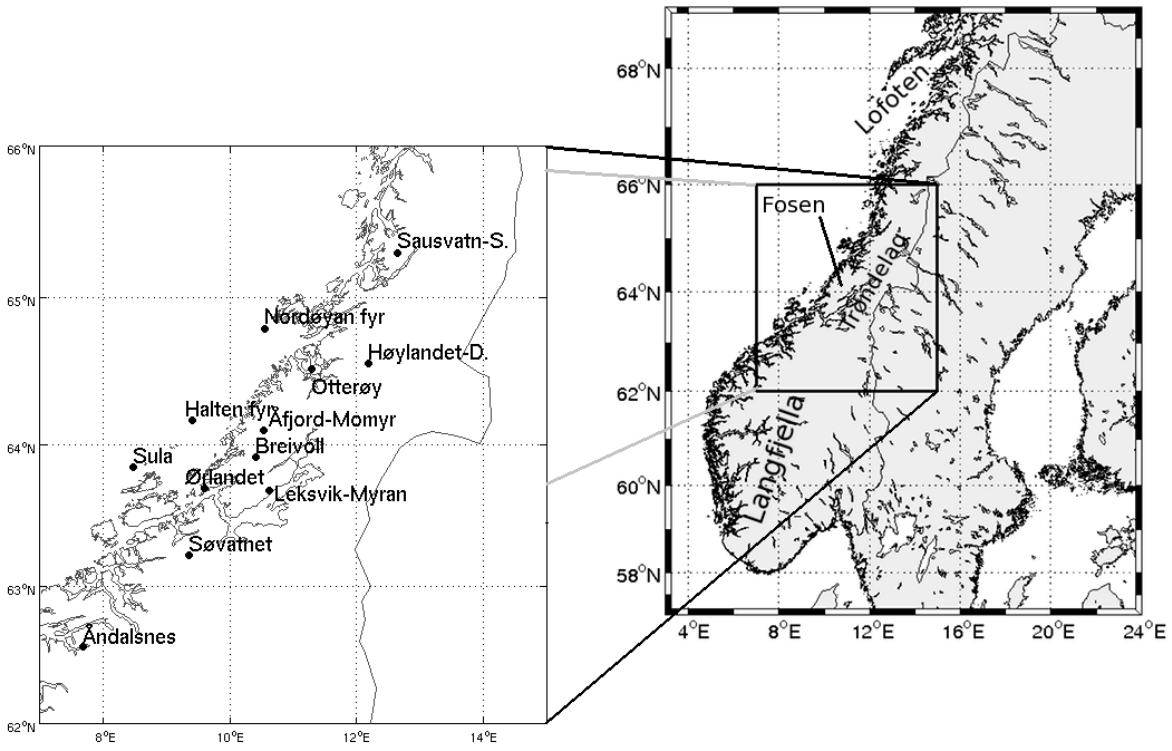

Figure 3: Map of the different stations and areas mentioned in the text.

Boundary and initial conditions are analysis from the European Centre for Medium-Range Weather Forecasts (ECMWF).

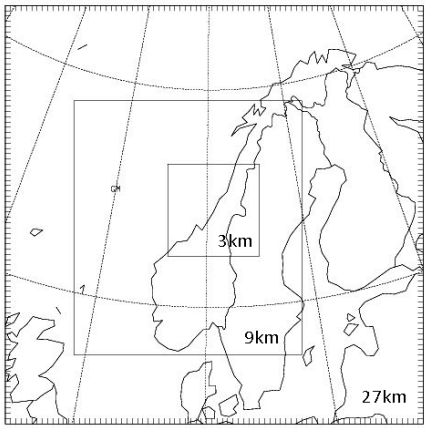

Figure 4: The 27, 9 and the 3 km domain.

The model was run with a horizontal grid cell resolution of 27, 9 and 3 km (see Figure 4 for domain locations). All the simulations were run with 29 vertical levels and with one-way nested domains. The control simulation (CTRL) starts at 00 UTC 29 January and runs for 120 hours until 00 UTC on 3 February. In addition, two sensitivity tests are simulated over the same time period, but with different parts of the topography removed. In the first sensitivity test all the topography south of Lofoten is removed, this run will be referred to as NOTOPO BIG. In the second, only the mountains in the southern part of Norway are removed. This mountain ridge is called Langfjella, and this sensitivity test

will be referred to as NOTOPO LANG. Figure 5 shows the different topography for the different runs in the 27 km domain.

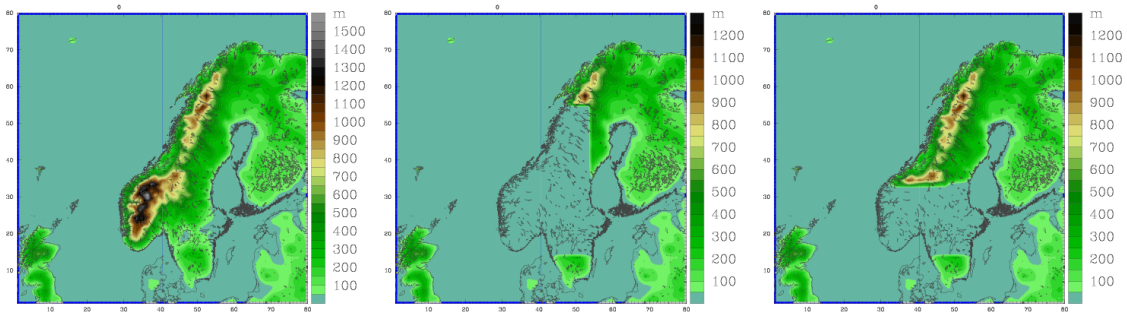

(a) CTRL **(b)** NOTOPO BIG **(c)** NOTOPO LANG

Figure 5: Topography in the 3 different simulations.

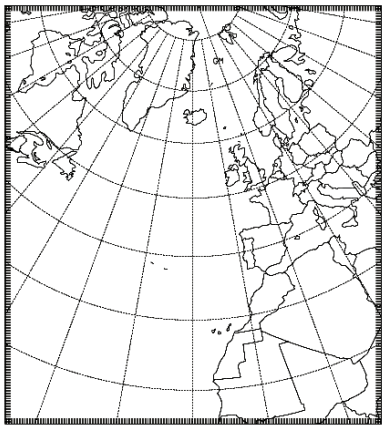

Figure 6: Domain with 27 km resolution for the forecast ability.

To test the predictability of this case several simulations with different initialisation times are carried out. Figure 6 shows the domain for these simulations, only a coarse domain of 27 km resolution is used and the domain includes a large part of the North Atlantic, East Canada, Europe and Northwest Africa. The longest simulation of this kind starts at 00 UTC on 25 January, there is one new simulation started every 24 hours until the 29 January. All these simulations end at 00 UTC 3 February.

4 Results

4.1 Validation

To validate the simulation of the event, precipitation measurements from weather stations taken at 06 UTC 31 January are compared with 24 hours accumulated precipitation for the same time period from the 3 km and 9 km domain in the CTRL simulation. Figure 7 shows the measured and modeled precipitation from 14 different stations. Overall, the simulation agrees quite well with the observations, except for Søvatnet and the four

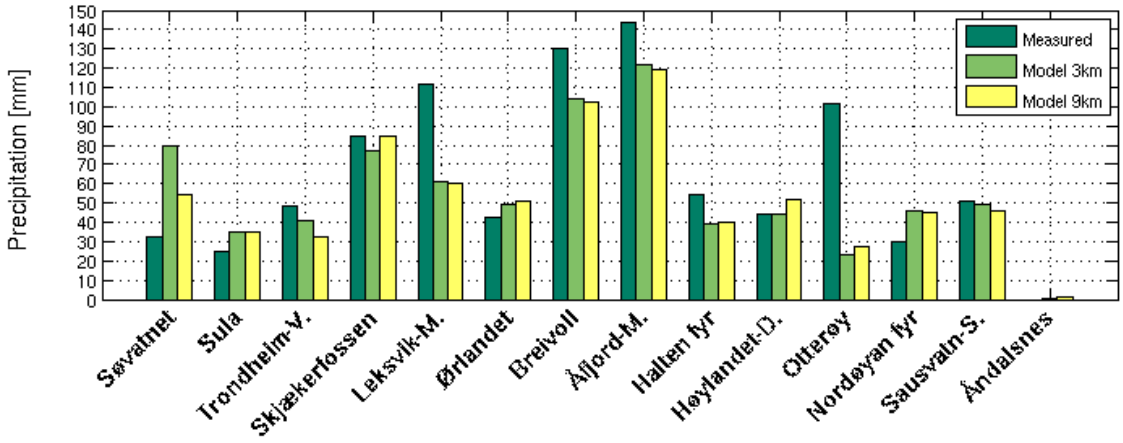

Figure 7: Measured and modeled precipitation from the 3 km and 9 km domain for 14 different stations.

stations with the highest measured precipitation. At Søvatnet, which is located 306 meters above sea level south of the extreme precipitation area, the model overestimates the measured precipitation by 48 mm/24h in the 3 km domain and 22 mm/24h in the 9 km domain. On the other hand, the model underestimates the precipitation at the four stations with the highest measured precipitation. Leksvik-Myran, Breivoll and Åfjord-Momyr are situated in the Fosen Peninsula. Leksvik-Myran, which is underestimated by 51 mm/24h in both domains, is located on the lee-side of the peninsula. The precipitation at Otterøy which is located just north of the peninsula, 36 meters above sea level, is underestimated by over 78 mm/24h in the 3 km domain and 74 mm/24h in the 9 km domain and this station is the worst represented by the model of all the stations used in this study. In spite of these differences, the overall quality of the simulation must be characterized as quite good.

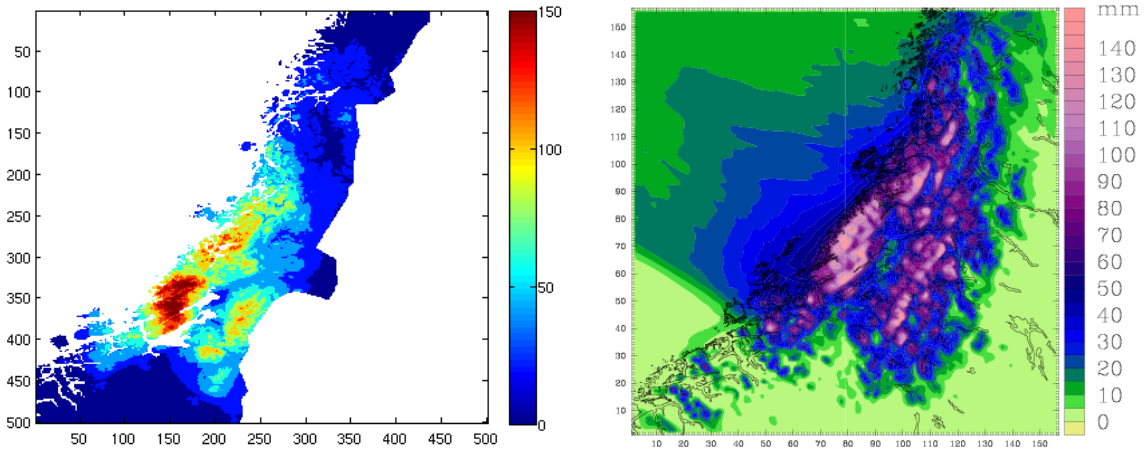

(a) **(b)**

Figure 8: a) Interpolated measured 24 hours accumulated precipitation with 1 km resolution (Mohr, 2008) from 0600 UTC 31 January 2006, b) modeled 24 hours accumulated precipitation in the 3 km domain CTRL run for the same time.

Figure 8 shows the measured and modeled precipitation field over Trøndelag. The ob-

served and gridded precipitation field is located more to the south than in the model, which corresponds to the overestimation at Søsvatnet.

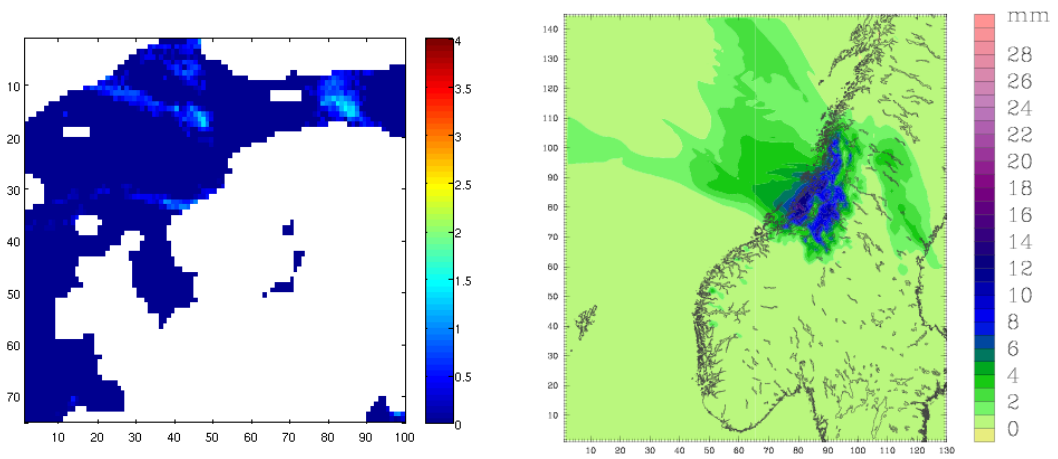

(a) **(b)**

Figure 9: a) Satellite precipitation data mm/h over Northern Europe for 30 January 12 UTC passes from the HOAPS archive, b) simulated precipitation mm/3h at 12 UTC 30 January from the 9 km domain.

Radar images are not available, but over the ocean, satellite observations of precipitation can be used to compare with the simulation (Figure 9 (a)). The satellite data are from the Hamburg Ocean Atmosphere Parameter (HOAPS) archive, it contains 1 degree twice daily multi-satellite composite products (Andersson *et al.* , 2007). The precipitation data are derived by passive microwave radiometers from the Special Sensor Microwave/Imager (SSM/I) (Wentz & Spencer, 1996). The grid-cells contain a composite of data from satellites that passed the grid box closest to 12 UTC and 24 UTC.

Figure 9 shows satellite precipitation data for the 12 UTC passes 30 January and 3 hours accumulated precipitation 12 UTC 30 January from the 9 km domain CTRL run. Both the satellite precipitation data and the modeled precipitation show low precipitation rates over the ocean.

4.2 The synoptic scale forcing

According to classic quasi-geostrophic theory, the ascending motion needed for precipitation is related to either differential advection of vorticity or advection of temperature and there is indeed consensus that most cases of heavy precipitation at middle to high latitudes in the winter are associated with fronts and upper level troughs. Figure 10 (a) og (b) show vorticity and the geopotential at 300 hPa, and temperature and wind at 850 hPa, respectively. The figures reveal that there is no advection of vorticity at a level where such advection should be expected and that there is only quite moderate advection of temperature at lower levels. The large scale forcing is in other words of very limited magnitude.

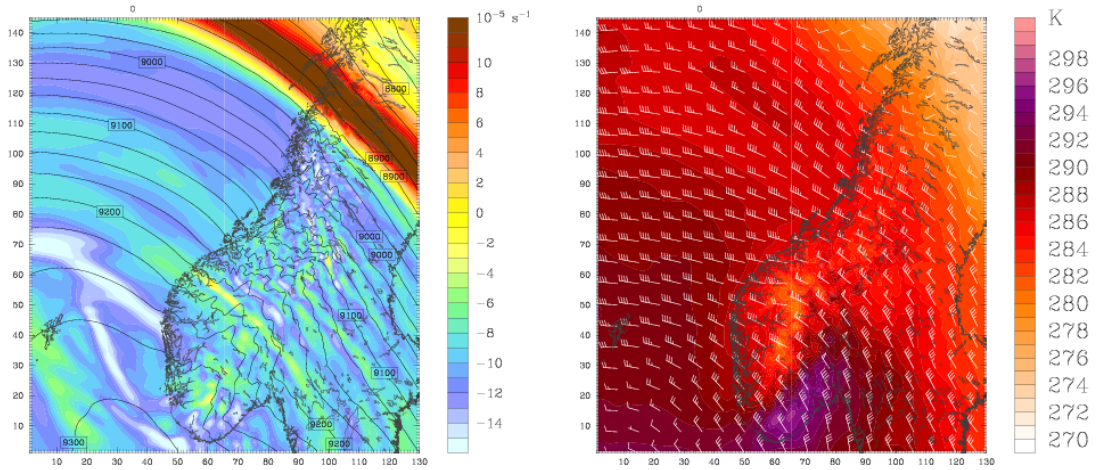

Figure 10: (a) Vorticity and geopotential height at 300 hPa with 25 m interval, (b) Potential temperature and wind vectors at 850 hPa, both at 18 UTC on 30 January in the 9 km domain

4.3 Sensitivity to Topography

The large difference in precipitation between land and the ocean gives a reason to simulate the event without topography. As mentioned above, two different simulations where done without topography.

Table 1 shows 3 hours accumulated precipitation at 12 UTC 30 January for 6 stations in the 3 km domain, see Figure 3 for the location of the stations.

Table 1: The difference between the topography simualtions

Model	Ørl.	Brei.	Åfjord.	Trond.	Skjæ.	Høyl.	Average
CTRL	4.5 *100 %*	10.5 *100 %*	14.4 *100 %*	4.0 *100 %*	10.2 *100 %*	5.8 *100 %*	7.8 *100 %*
NOTOPO LANG	5.6 *124.6*	8.0 *76.0 %*	9.0 *62.7 %*	3.2 *80.4 %*	7.0 *69.0 %*	3.2 *55.0 %*	5.7 *73.1 %*
NOTOPO BIG	3.1 *69.0 %*	4.0 *38.3 %*	4.1 *28.3 %*	2.3 *59.6 %*	2.2 *21.3 %*	1.8 *31.4 %*	2.9 *37.2 %*

3 hour accumulated precipitation for 30 January 12 UTC for the 3 different topography simulations from the 3 km domain.

There is a clear influence of topography. The simulation where most of the topography of Scandinavia is removed (NOTOPO BIG) produced about one third of the precipitation in the CTRL simulation, and the precipitation rates have less variation between the different stations. For the Ørlandet station, the NOTOPO LANG simulation produces more precipitation than the CTRL run. Yet for the other stations the precipitation rates decreases between 50 - 20 % from the CTRL simulation. The different precipitation pattern between the CTRL and NOTOPO LANG simulation shows that the topography in Southern Norway can significantly affect the flow pattern over Central Norway (Trøndelag).

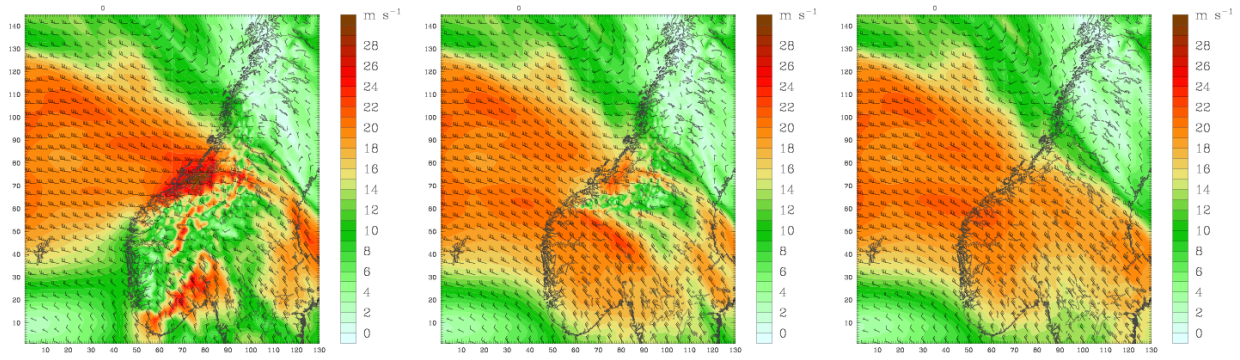

(a) CTRL **(b)** NOTOPO LANG **(c)** NOTOPO BIG

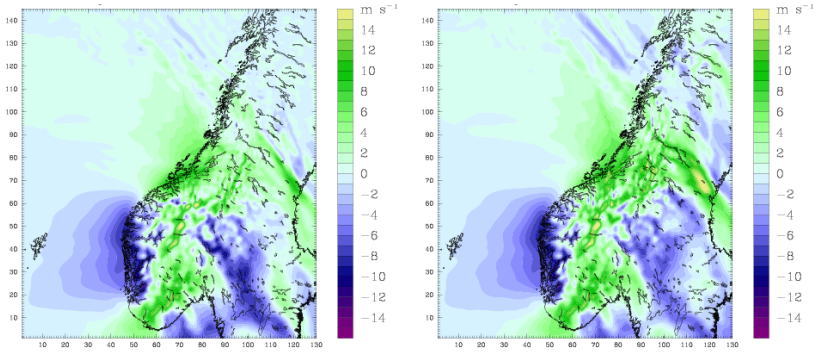

(d) CTRL - NOTOPO LANG **(e)** CTRL - NOTOPO BIG

Figure 11: (a-c) winds at 925 hPa in the 9 km domain on 30 January at 12 UTC for the CTRL, NOTOPO LANG and NOTOPO BIG, (d) difference in wind speed between CTRL and NOTOPO LANG and (e) the CTRL and NOTOPO BIG difference.

Figure 11 (a)-(c) show the wind pattern in the 9 km domain at 925 hPa on 30 January 12 UTC for the different topography simulations, and (d)-(e) show the difference between the CTRL and the other topography simulations. The CTRL simulation has the greatest wind speed over Central Norway, about 8 m/s greater than the NOTOPO LANG and NOTOPO BIG simulations. The wind direction in the CTRL run is more westerly than for the two other simulations. Both the NOTOPO simulations give much stronger winds than the CTRL simulation at the west coast of Norway, south of our area of interest. It is evident that the Langfjella mountain ridge acts as a blocking for the flows over Southern Norway and increases the wind speed in Central Norway.

4.4 The Origin of the Air Masses

Trajectories are calculated by the HYSPLIT trajectory model using Reanalysis data from NOAA (Draxler & Rolph, 2010; Rolph, 2010). Figure 2(b) shows that the highest measured precipitation rates were between 06 UTC 29 January and 06 UTC 1 February. Trajectories are calculated backwards over 120 hours with 6 hour intervals between each trajectory for this time period. Figure 12(a) and (b) show 13 trajectories for air parcels ending over the Fosen peninsula. All the trajectories at both altitudes have a route between the British Isles and Iceland before the air parcels reach the coast of Central Norway. The red trajectories from the beginning and the end of the period originate at around

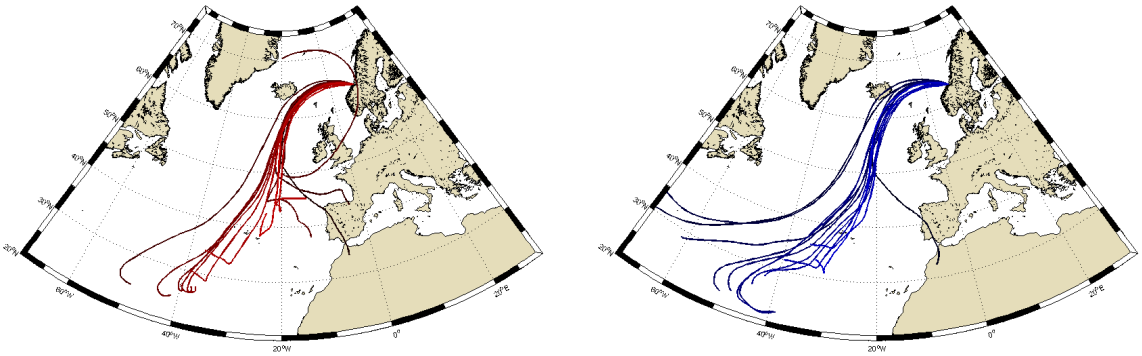

(a) **(b)**

Figure 12: Trajectories for different air parcels starting at 06 UTC on 29 January and ending over the Fosen peninsula at 06 UTC on 1 February with 6 hours interval. The darkest trajectories are from the beginning of the period and they become lighter towards the end. (a) Parcels stopping 3500 m above the peninsula and (b) 5000 m above.

40°N, and one is caught in the anticyclone over the British Isles. However the majority of the red trajectories and all of the blue trajectories which are at higher altitudes, originate at subtropical latitudes. The warm moist air parcels that follow these trajectories travel over 40°of latitude northwards before ending up over the Fosen peninsula.

4.5 Sensitivity to Initial Conditions

To assess the forecast quality as a function of lead time, 5 simulations with different initial time are run over a large domain. Figure 13 shows the precipitation produced by the model with the different initial times. Figure 13(a) and (b) shows the mean 24 hours accumulated precipitation 06 UTC 31 January in mm and percent of the observed, respectively, for 5 different stations. Figure 13(c) and (d) show the mean 1 hour accumulated precipitation in mm and percent for 9 different points over the ocean. There is an almost linear decrease with increased lead time in the forecasted precipitation over land, while over the ocean the three model runs with the latest initial time produce fairly similar amounts, and the simulation starting at 00 UTC on 26 January produces very little precipitation.

Comparing the two simulations, initialized at 00 UTC on 28 January and at 00 UTC on 29 January, it is clear that both simulations are similar over the ocean, while the one initialized later (shorter lead time) does better in reproducing the enhancement of the precipitation over land. In the following, we shall concentrate on the difference between these two simulations, in order to shed a light on why the forecast with the longer lead time did worse in reproducing precipitation over land. From now on the simulation initialized at 00 UTC on 28 January will be referred to as BAD, while the simulation initalized at 00 UTC on 29 January will be referred to as GOOD. Figure 14 shows the time series of the GOOD and BAD simulations.

Figure 15 shows the wind field at 850 hPa in the GOOD simulation and the difference between the GOOD and the BAD simulation at 12 UTC on 30 January. In Central-Norway, the winds are strong and in the GOOD simulation they are about 8 m/s stronger than in the BAD simulation.

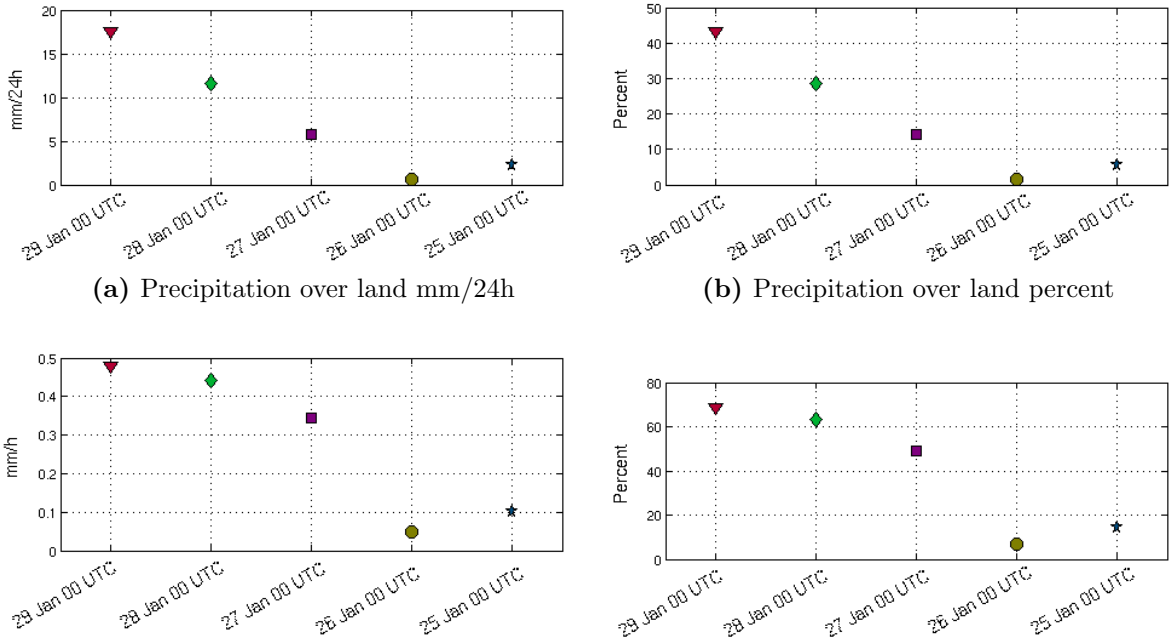

(a) Precipitation over land mm/24h

(b) Precipitation over land percent

(c) Precipitation over ocean mm/1h

(d) Precipitation over ocean percent

Figure 13: Precipitation produced by the model for different lead times for the big 27 km domain. (a) Mean 24 hours accumulated precipitation at 06 UTC on 31 January for Ørlandet, Sula, Halten fyr, Trondheim Voll and Åfjord-Momyr in mm and (b) percent of observed precipitation at the same stations. (c) Mean 1 hour accumulated precipitation from 9 different points over the ocean from 30 January 06 UTC to 18 UTC and (d) percent of observed precipitation from the HOAPS data archive for the passes closest to 30 January 12 UTC.

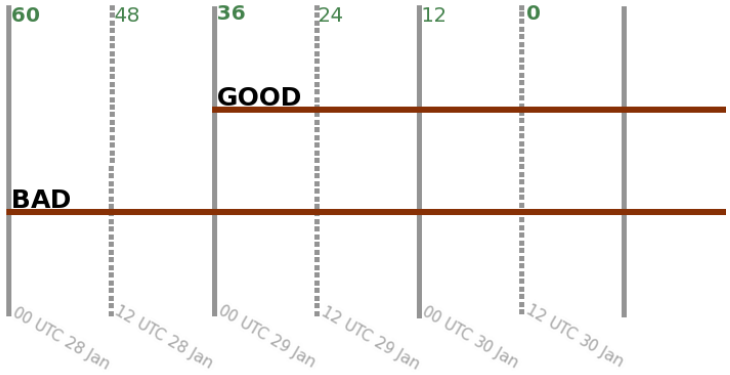

Figure 14: Timeline of the GOOD and the BAD simulations. The green numbers above are hours before 12 UTC 30 January.

The low level winds are close to geostrophic and in order to explore the origin of the difference in the wind fields, it is convenient to trace the differences between these two simulations in the surface pressure field (Figure 16).

At the initial time for the GOOD simulation this simulation has lower pressure between Greenland and Iceland (Figure 16(a)). The circle shows how the depression moves east,

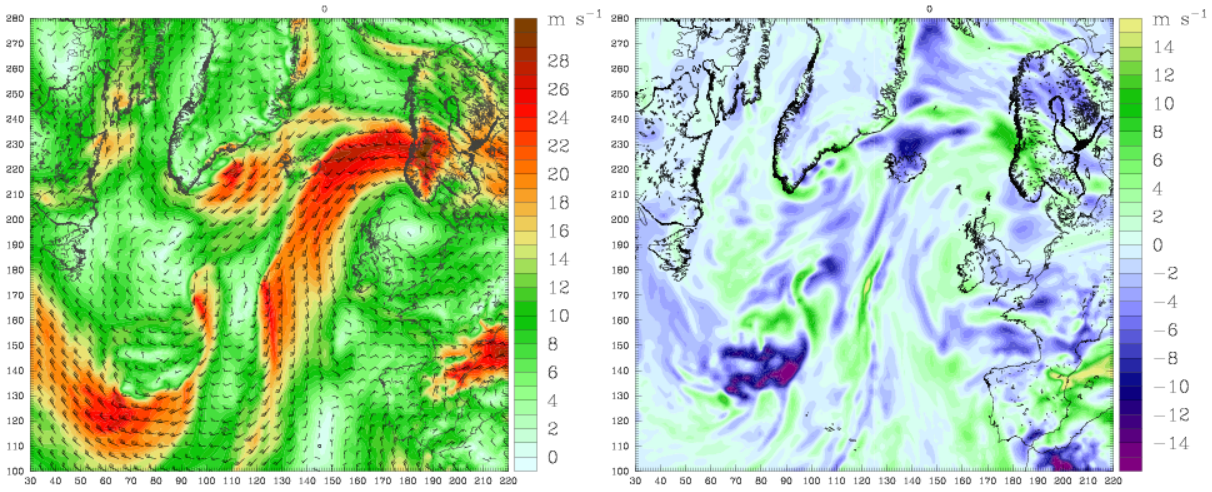

(a) **(b)**

Figure 15: (a) Wind field at 850 hPa 1 at 2 UTC on 30 January in the GOOD simulation, and (b) the difference wind field (GOOD-BAD) at the same time.

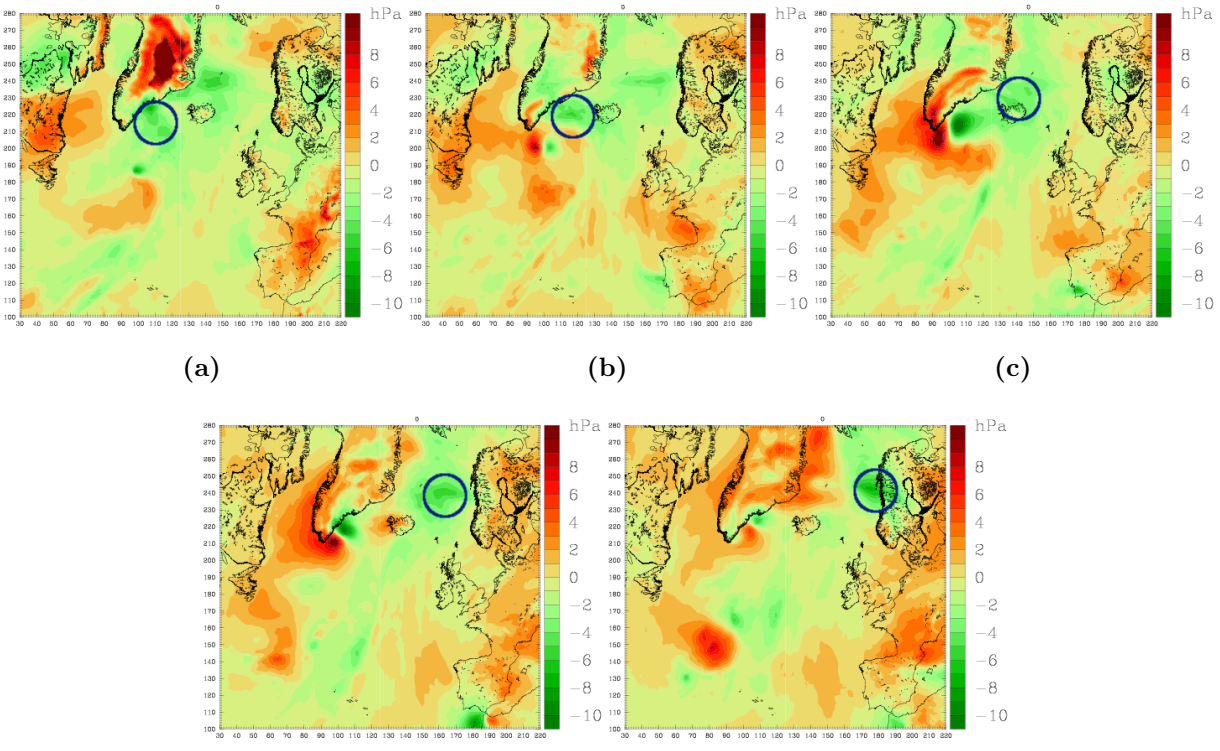

(a) **(b)** **(c)**

(d) **(e)**

Figure 16: The difference MSLP between the BOOD and the BAD simulations (GOOD-BAD) with 9 h intervals (a) 00 UTC 29 January, (b) 09 UTC 29 January, (c) 18 UTC 30 January, (d) 03 UTC 30 January, and (e) 12 UTC 30 January. The circle shows the depression.

and at 12 UTC on 30 January the depression is located over Trøndelag.

The lower pressure in the GOOD simulation is associated with higher low-level tempera-

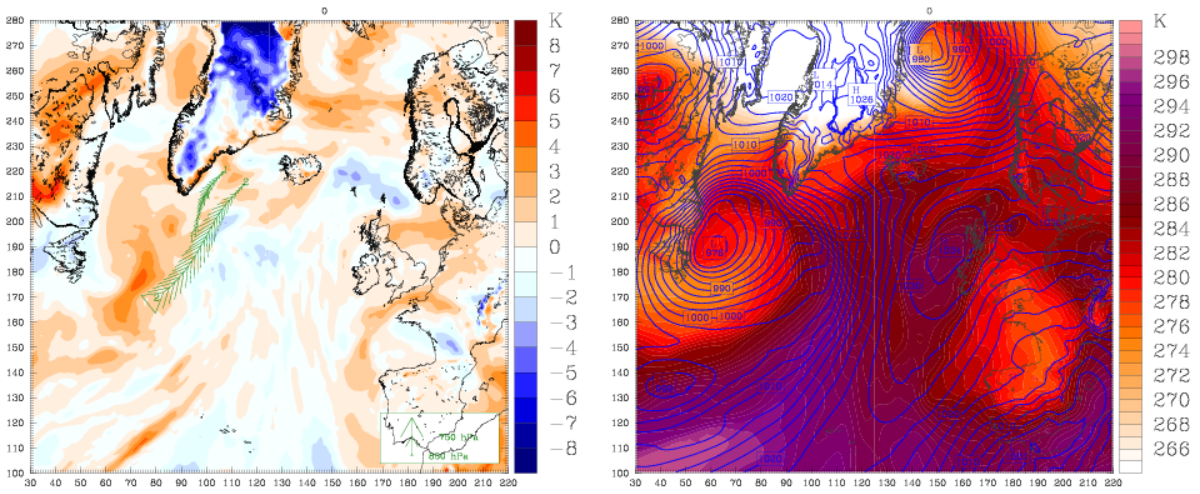

(a) **(b)**

Figure 17: (a) Difference field between GOOD and BAD (GOOD -BAD) potential temperature at 850 hPa at 00 UTC on 29 January and trajectories from 00 UTC on 28 January to 00 UTC 29 January. (b) Potential temperature in 850 hPa and MSLP with 2.5 hPa interval 00 UTC 28 January.

tures than in the BAD simulation. Figure 17 (a) shows the differential temperature field between the GOOD and the BAD forecast at 850 hPa at 00 UTC on 29 January, and trajectories starting 24 hours earlier and ending inside the temperature anomaly at 850 hPa on 00 UTC 29 January. Both trajectories lead directly to the region of the cold front, suggesting very strongly that the temperature where the GOOD and the BAD simulations differ from each other is sensitive to the baroclinic development south of Greenland.

5 Discussion

Perhaps the most interesting result of this study, is how the topography of Southern Norway (Langfjella) contributes to the precipitation in regions far away from the mountains. Due to the Coriolis force, the flow symmetry around a mountain ridge is broken, and an increase of the flow occurs on the left side (e.g. Ólafsson & Bougeault (1997)). The increased flow, in this case on the northern side of the range, causes increased forcing, that lead to increased precipitation. Increased vertical velocities and precipitation on this side of a mountain range are also explored in Ólafsson (2000) and Hunt *et al.* (2001). However, in these two studies, the increased lifting was due only to asymmetry in the flow field and not direct lifting by the increased wind impinging the mountains, as in this case. Ólafsson & Bougeault (1996) discovered that increased wind speed at the edge of a mountain range contributed to enhanced breaking of gravity waves on the flanks of the mountain, and called it secondary wave breaking. In line with this, we call the topographic effect from Langfjella a secondary topographic forcing of precipitation generation. The primary effect is the direct lifting of the air masses when impinging a mountain.

It is also of interest that very much of the precipitation is generated locally, by the strong flow impinging the mountains. This is in contrast to most precipitation systems in this

part of the world, where fronts and upper level vorticity advection are the important factors. This case is an example of an extreme that is fundamentally different from many non-extreme cases in terms of atmospheric dynamics. A result of this kind should be considered when statistically modeling the distribution of events of allegedly the same kind.

As in the study of Stohl *et al.* (2008), the air masses originate from the subtropics. In the case of Stohl *et al.* (2008), the transport was associated with two tropical hurricanes that underwent transition to extratropical cyclones. Occurring as late as at the end of January, no hurricanes were present in this case. A main point of interest in this context may be that in spite of the precipitation being generated by perturbations on mesoscale, a certain large scale quasi-stationary flow pattern is needed.

The large spatial variability in the precipitation in the present case is not surprising and must be related to variability in the small-scale forcing as described for instance in Reuder *et al.* (2007) for flow over complex topography in Western Norway.

Einarsson *et al.* (2004) investigated a case of a summer-time extreme precipitation in Central Norway and found the predictability of the event to be sensitive to low level winds. In spite of the Einarsson case being a summer event of quite a convective nature, it resembles the present case in the aspect of being sensitive to the low level winds impinging the topography.

In this paper, we present quite a novel approach to assessing what goes wrong in a forecast. A similar approach has been introduced in the thesis' of Hagen (2008); Tveita (2008). Drawing very conclusive conclusions from tracing back air masses in a region where a new analysis gives a field that is different from a 24 hour forecast can of course be questioned. The result, leading us to an upstream baroclinic zone in however in agreement with a common result of sensitivity area predictions pointing at areas in the baroclinic zone below the jet, upstream of the verification areas, indicating that improved observations in these zones may lead to better forecasts downstream (e.g. Rabier *et al.* (1996)).

A final point of interest is the fact that during this winter season, the NAO index was negative. In such conditions, mean precipitation should be expected to be less than average in Central Norway. Yet, the present case has extreme precipitation. This underlines the fact that individual extreme events, even though they may last for several days do not necessarily follow mean seasonal values.

6 Summary and conclusions

The main conclusions of the present study is that the extreme precipitation event during winter 2006 in Central Norway was to large extent generated by local topographic forcing, even though the precipitation extended over a large area and the air masses originated in the sub-tropics. The dominating topographic effect was direct lifting of the impinging air masses, while a secondary topographic effect was the enhancement of the speed of the impinging flow due to deflection away from a mountain range to the south of the area of extreme precipitation. Finally, an accurate prediction of the winds in Central Norway may be dependent on the representation of a baroclinic system to the southeast of Newfoundland three days earlier.

Acknowledgements

The authors gratefully acknowledge the NOAA Air Resources Laboratory (ARL) for the provision of the HYSPLIT transport and dispersion model used in this publication and READY website (http://www.arl.noaa.gov/ready.php) used in this publication. The authors are also grateful for the HOAPS satellite data provided trough the CERA database by Axel Andersson at the Centre for Marine and Atmospheric Sciences (ZMAW), Germany, and the gridded precipitation maps from senorge.no provided by Matthias Mohr from the Norwegian Meteorology Institute.

References

Andersson, A., Bakan, S., Fennig, F., Grassl, H., Klepp, C.H., & Schulz, J. 2007. *Hamburg Ocean Atmosphere Parameters and Fluxes from Satellite Data - HOAPS-3 - twice daily composite.* [doi: 10.1594/WDCC/HOAPS3_DAILY].

Beldring, S., Engen-Skaugen, T., Førland, E. J., & Roald, L. A. 2008. Climate change impacts on hydrological processes in Norway based on two methods for transferring regional climate model results to meteorological station sites. *Tellus A*, **60**, 439–450.

Benestad, R. E., & Haugen, J. E. 2007. On complex extremes: flood hazards and combined high spring-time precipitation and temperature in Norway. *Climatic Change*, **85**, 381–406.

Draxler, R. R., & Rolph, G. D. 2010. HYSPLIT (HYbrid Single-Particle Lagrangian Integrated Trajectory) Model access via NOAA ARL READY Website (http://ready.arl.noaa.gov/HYSPLIT.php). *NOAA Air Resources Laboratory, Silver Spring, MD.*

Einarsson, E. M., Ólafsson, H., & Kristjansson, J. E. 2004. Forecasting an extreme precipitation event in Norway. *11th Conference on Mountain Meteorology and the Annual Mesoscale Alpine Program (MAP).*

Hagen, B. 2008 (June). *Wind extremes in the Nordic Seas - Dynamics and forecasting.* M.Phil. thesis, Geophysical Institute, University of Bergen.

Hanssen-Bauer, I., Førland, E.J., Haugen, J.E., & Tveito, O. E. 2003. Temperature and precipitation scenarios for Norway: comparison of results from dynamical and empirical downscaling. *Climate Research*, **25**, 15.

Haugen, J. E., & Iversen, T. 2008. Response in extremes of daily precipitation and wind from a downscaled multi-model ensemble of anthropogenic global climate change scenarios. *Tellus Series a-Dynamic Meteorology and Oceanography*, **60**, 411–426.

Hunt, J. C. R., Ólafsson, H., & Bougeault, P. 2001. Coriolis effects on orographic and mesoscale flows. *Quarterly Journal of the Royal Meteorological Society*, **127**, 601–633.

Mohr, M. 2008. *New Routines for Gridding of Temperature and Precipitation Observations for "seNorge.no".* p. 40. Met.no Report.

Ólafsson, H. 2000. The impact of flow regimes on asymmetry of orographic drag at moder-

ate and low Rossby numbers. *Tellus. Series A, Dynamic meteorology and oceanography*, **52**, 365–379.

Ólafsson, H., & Bougeault, P. 1996. Nonlinear flow past an elliptic mounatin ridge. *Journal of Atmospheric Sciences*, **53**, 2465–2489.

Ólafsson, H., & Bougeault, P. 1997. The effect of rotation and surface friction on orographic drag. *Journal of Atmospheric Sciences*, **54**, 193–210.

Rabier, F., Klinker, E., Courtier, P., & Hollingsworth, A. 1996. Sensitivity of forecast errors to initial conditions. *Quarterly journal of the Royal Meteorological Society*, **122**, 121 – 150.

Reuder, J., Fagerlid, G. O., Barstad, I., & Sandvik, A. 2007. Stord Orographic Precipitation Experiment(STOPEX): an overview of phase I. *Advances in Geosciences*, **10**, 17–23.

Rolph, G.D. 2010. Real-time Environmental Applications and Display sYstem (READY) Website (http://ready.arl.noaa.gov). *NOAA Air Resources Laboratory, Silver Spring, MD.*

Skamarock. 2008. A Description of the Advanced Research WRF Version 3. *Ncar technical Note*, p. 125.

Stohl, A., Forster, C., & Sodemann, H. 2008. Remote sources of water vapor forming precipitation on the Norwegian west coast at 60°N - a tale of hurricanes and an atmospheric river. *Journal of Geophysical Research-Atmospheres*, **113**, D05102, doi:10.1029/2007JD009006.

Tveita, B. 2008 (June). *Extreme winds in the Nordic Seas - An observational and numeical study.* M.Phil. thesis, Geophysical Institute, University of Bergen.

Wentz, F. J., & Spencer, R. W. 1996. SSM/I Rain Within an Unified All-Weather Ocean Alorithm. *Journal of the Atmospheric Sciences*, **55**, 1613–1627.

Chapter 8

Summary and general conclusions

In this thesis an extreme precipitation event over Central Norway in 2006 is studied. Topographic lifting of the impinging flow by the mountains in Central Norway is found to be the main cause of the extreme precipitation. This direct lifting of the impinging air is called the primary topographic effect. A secondary topographic effect is found to be the blocking of the flow over Southern Norway by the mountain ridge in this part of the country. The flow over Southern Norway is to a great extent diverted to the flanks of this ridge, instead of over it. The Coriolis force enhances this effect on the left side (facing downwind) of the mountain. The increased flow speed on the left side, in this case to the north contributes to the increased topographic forcing over Central Norway and produces a precipitation increase.

Both of the previously mentioned effects are local topographical effects, i.e. on a smaller scale than the synoptic scale flow that is the most common cause of precipitation in this part of the World. However the large scale circulation is also found important for the transportation of warm air masses from the sub-tropics.

A study on the predictability of the event shows that a 60 hour forecast manages to recreate the synoptic scale circulation, but there is a substantial improvement in the mesoscale forcing between forecasts with lead times of 60 hours and 30 hours. The error in the 60 hour forecast can be traced back to a baroclinic zone upstream of the extreme event.

A study is done on the probability for similar extreme precipitation events in present climate and a projection of future climate. An increase is found in the probability of

events of this kind in the climate model that is forced by a future greenhouse scenario. The increase in probability is higher during wintertime than in the summer. An increase in wintertime extreme events may potentially cause more damage due to snow-melting and increased run-off. In this study, the probability of individual weather parameters as well as a combination of several weather parameters has been studied. The result of such combination may not necessarily show the same tendency as for a sole parameter. The model shows that the frequency of heavy precipitation is reduced in the winter, while a combination of more parameters indicates an increase in the type of extreme precipitation events studied here.

There was a negative NAO index during the 2006 winter season when the event occurred. In such conditions the precipitation should be expected to be less than average in Central Norway. This underlines the fact that individual extreme events, even though they last over several days do not necessarily follow mean seasonal values.

Chapter 9

Future work

In complex terrain the precipitation field has large spatial variability. A more dense observation network or remote sensing can highlight these effects further. The present study has underlined the importance of knowing winds to describe the precipitation patterns in complex terrain. Future studies of precipitation in an environment like in Central Norway must therefore focus on local winds. The warm moist air that caused the heavy precipitation during the event are traced back to the sub-tropics. To put this event into perspective a more extensive tracking of moist particles causing precipitation over Central Norway could be done.

There are shortcomings in the model used here concerning its ability to recreate the observed wind data. There are also other uncertainties in this study due to the unresolved topography. Only one future greenhouse gas scenario is studied, a comparison between other scenarios can provide a better understanding of the future climate.

Appendix A

Synoptic situation figures

Geopotential height at 500 hPa.

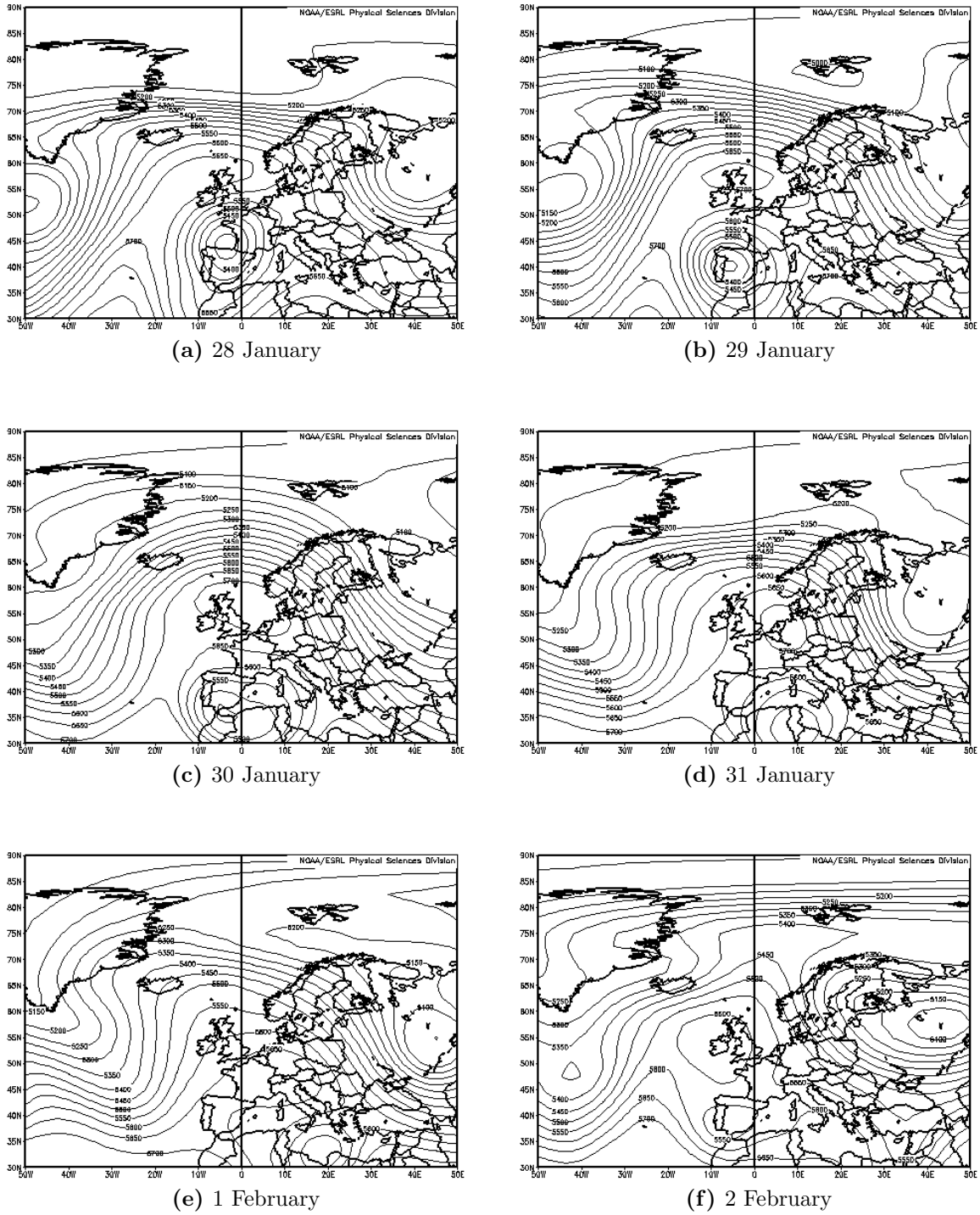

(a) 28 January **(b)** 29 January

(c) 30 January **(d)** 31 January

(e) 1 February **(f)** 2 February

Figure A.1: Mean geopotential height [m] at 500 hPa for each day, 50 m interval. Data from NCEP/Ncar, acquired through NOAA/CDC.

Geopotential height at 500 hPa, anomaly from the climatology mean.

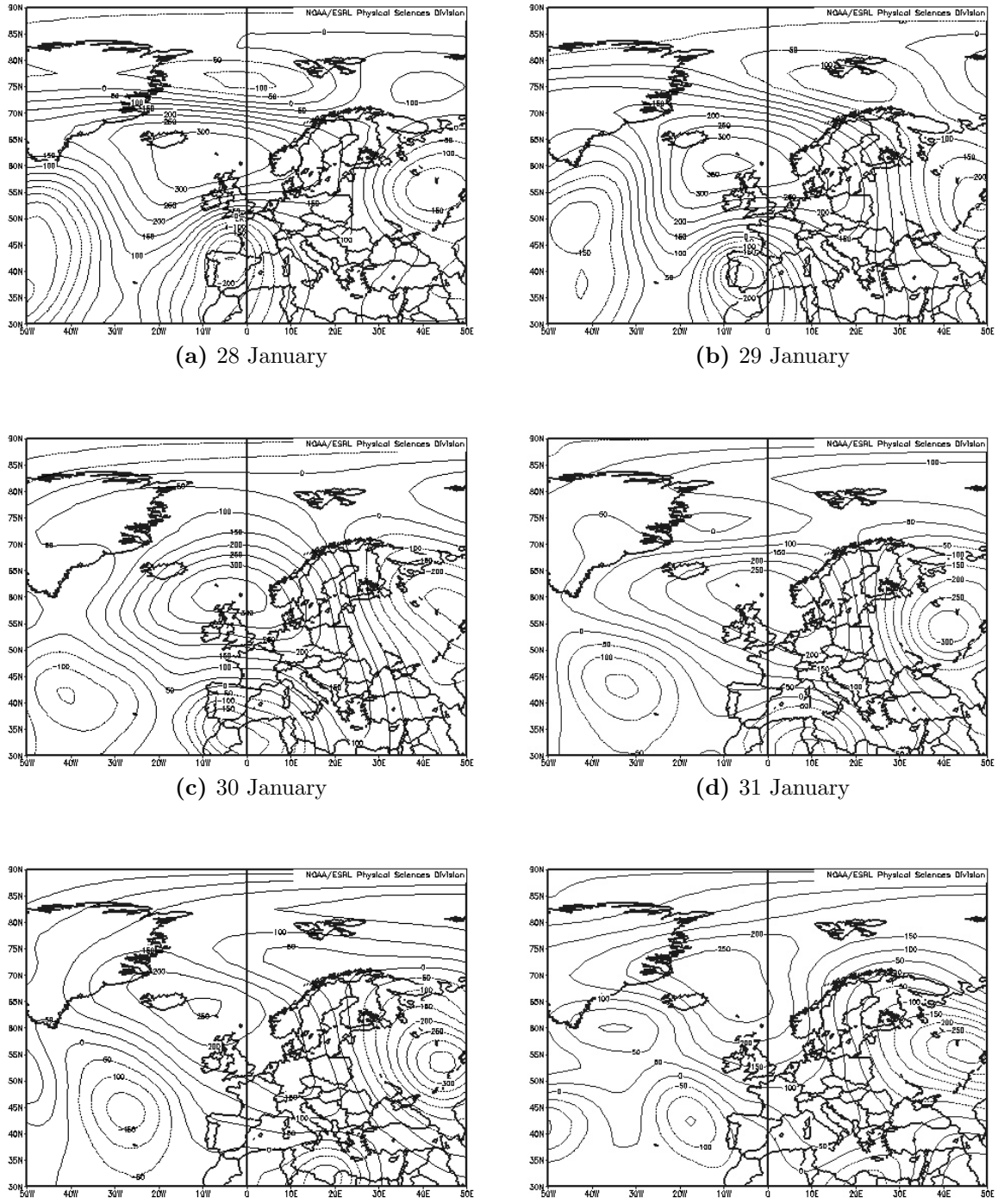

(a) 28 January **(b)** 29 January

(c) 30 January **(d)** 31 January

(e) 1 February **(f)** 2 February

Figure A.2: Geopotential height anomaly [m] from the climatology mean (1968-1996) at 500 hPa for each day, 50 m interval. Data from NCEP/Ncar, acquired through NOAA/CDC.

Air temperature at 500 hPa, anomaly from climatology average.

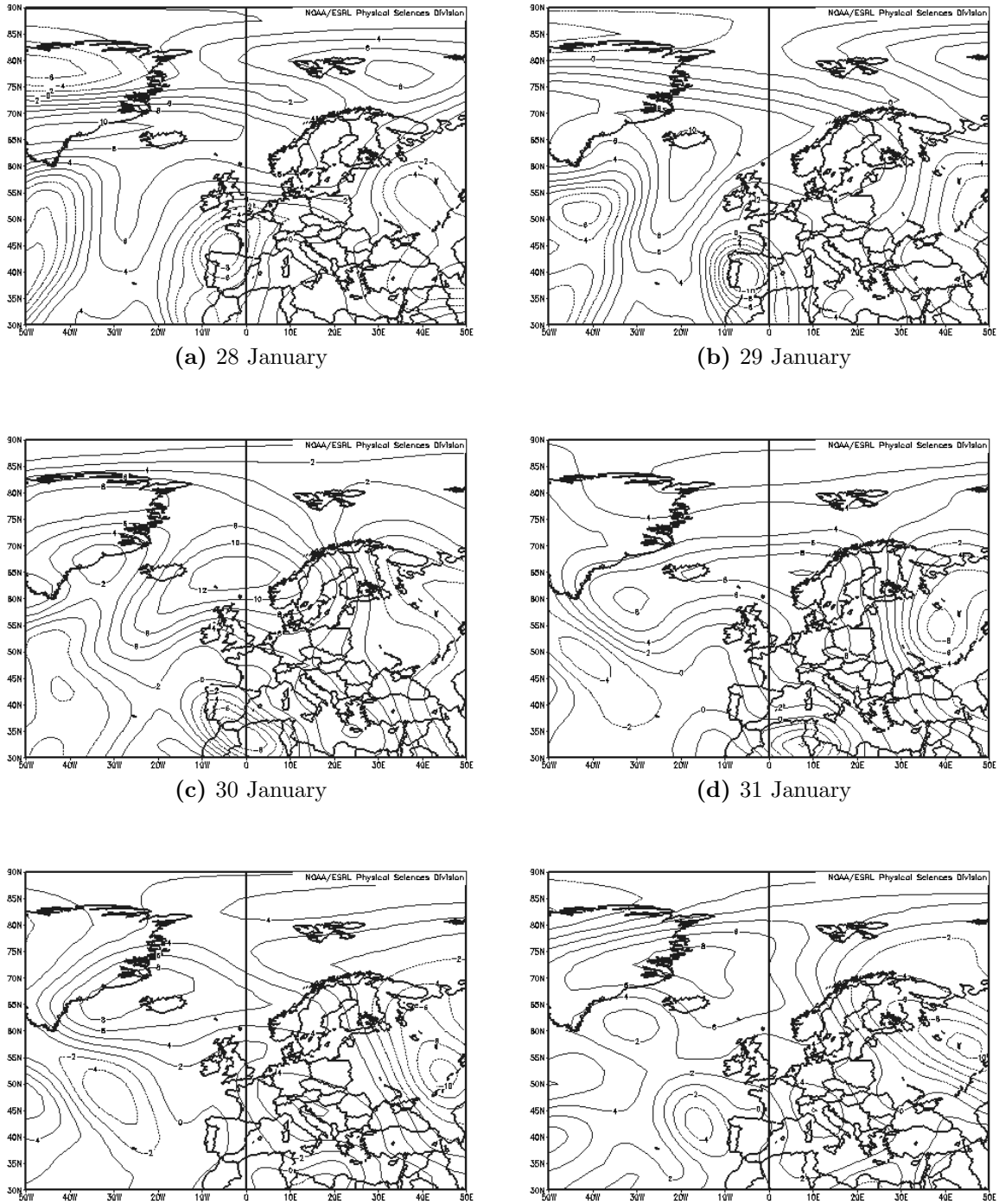

(a) 28 January **(b)** 29 January

(c) 30 January **(d)** 31 January

(e) 1 February **(f)** 2 February

Figure A.3: Air temperature anomaly from the climatology mean (1968-1996) at 500 hPa for each day, 2°K interval. Data from NCEP/Ncar, acquired through NOAA/CDC.

Air temperature at 850 hPa, anomaly from climatology average.

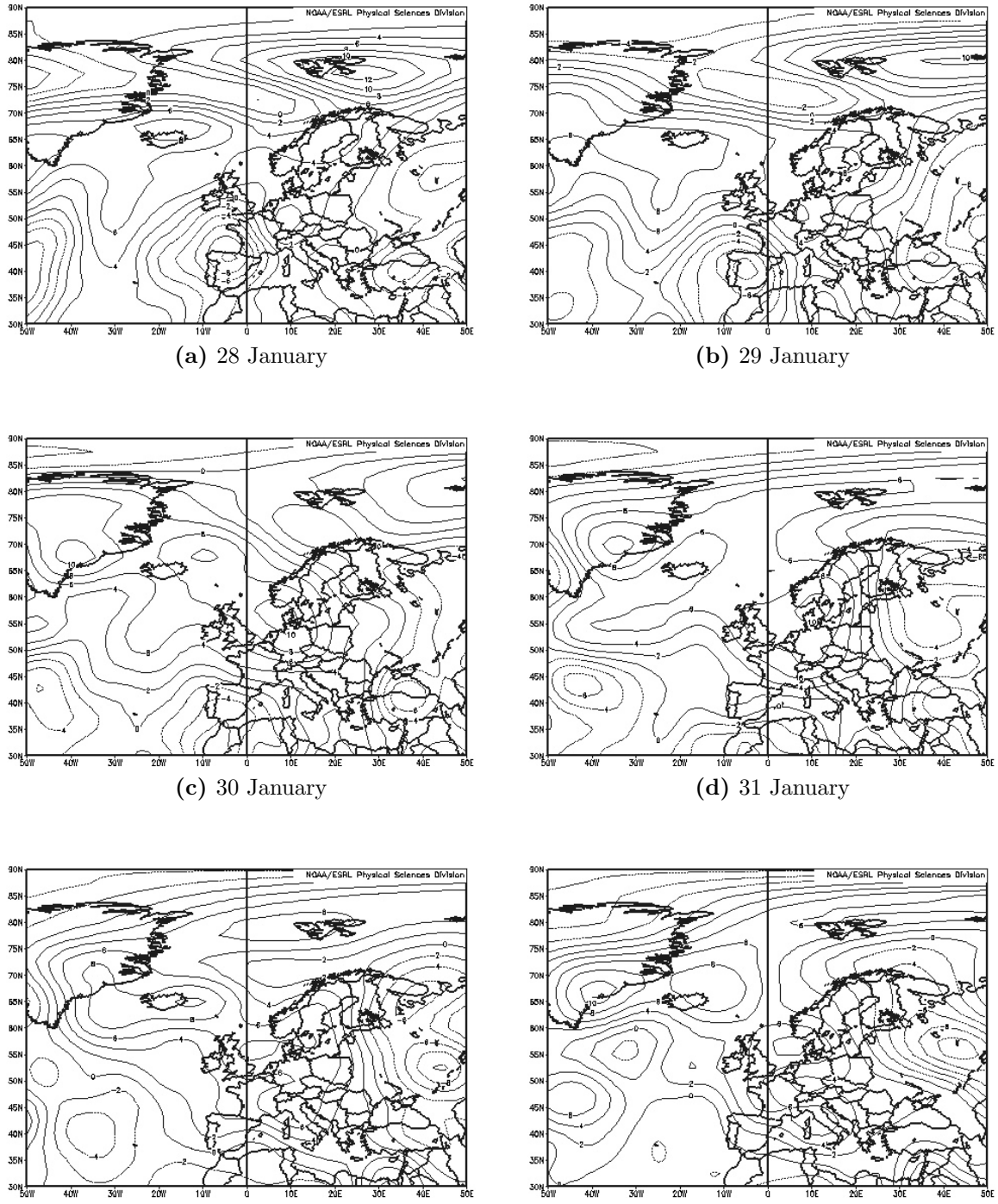

(a) 28 January **(b)** 29 January

(c) 30 January **(d)** 31 January

(e) 1 February **(f)** 2 February

Figure A.4: Air temperature anomaly from the climatology mean (1968-1996) at 850 hPa for each day, 2°K interval. Data from NCEP/Ncar, acquired through NOAA/CDC.

Surface analysis with observations

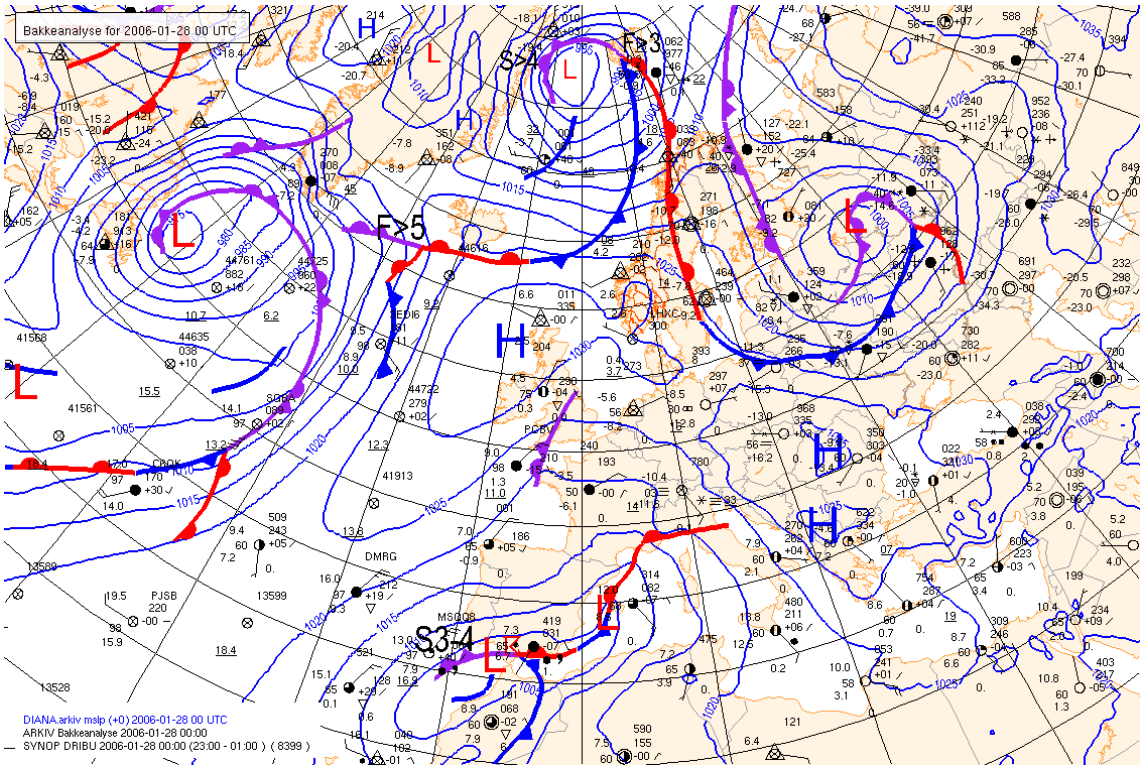

(a) 00 UTC 28 January

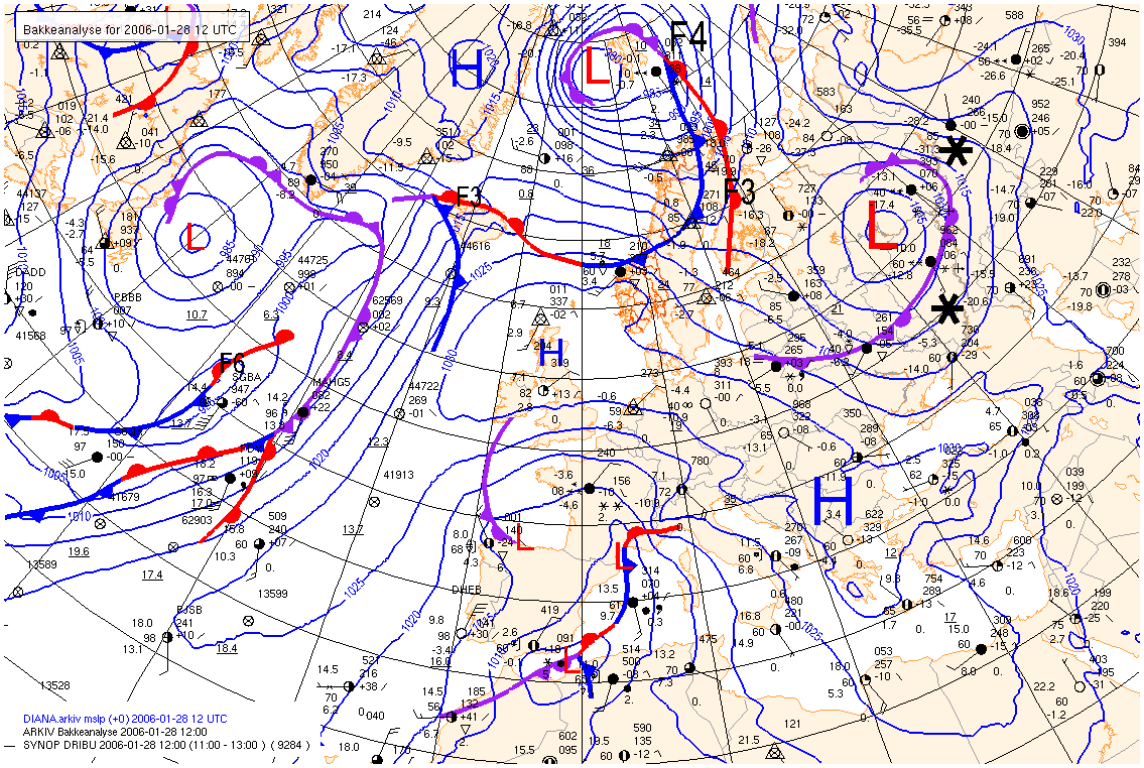

(b) 12 UTC 28 January

Figure A.5

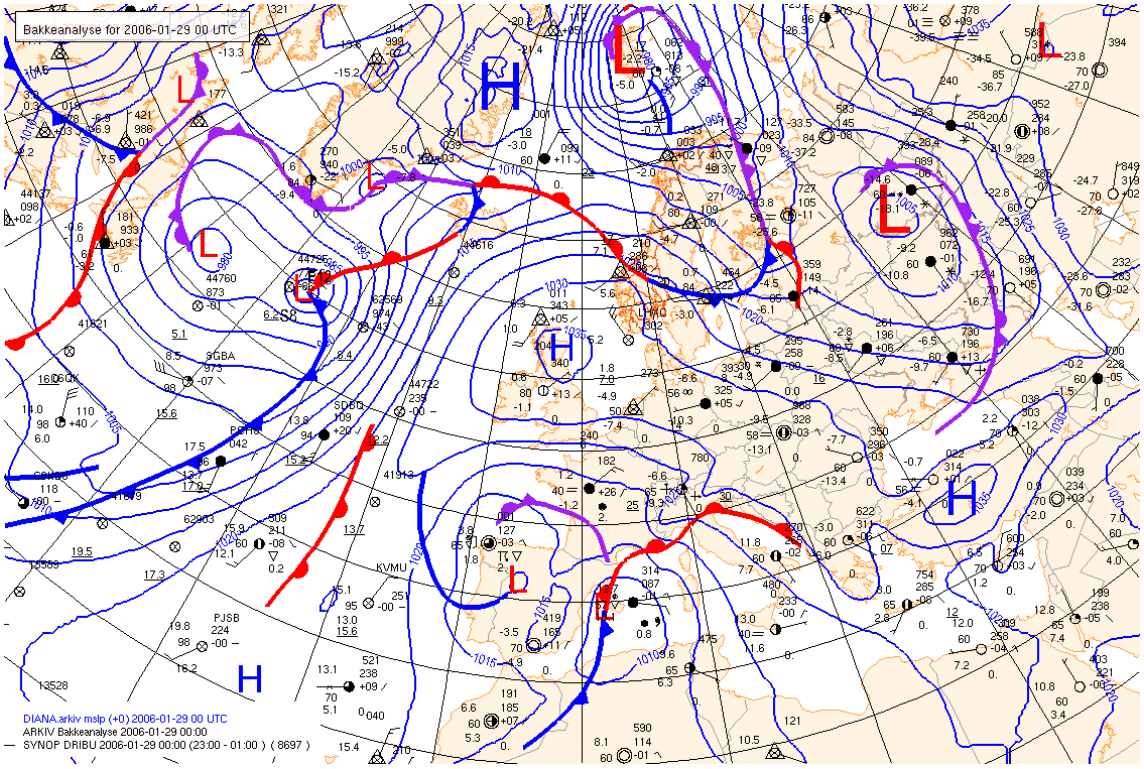

(c) 00 UTC 29 January

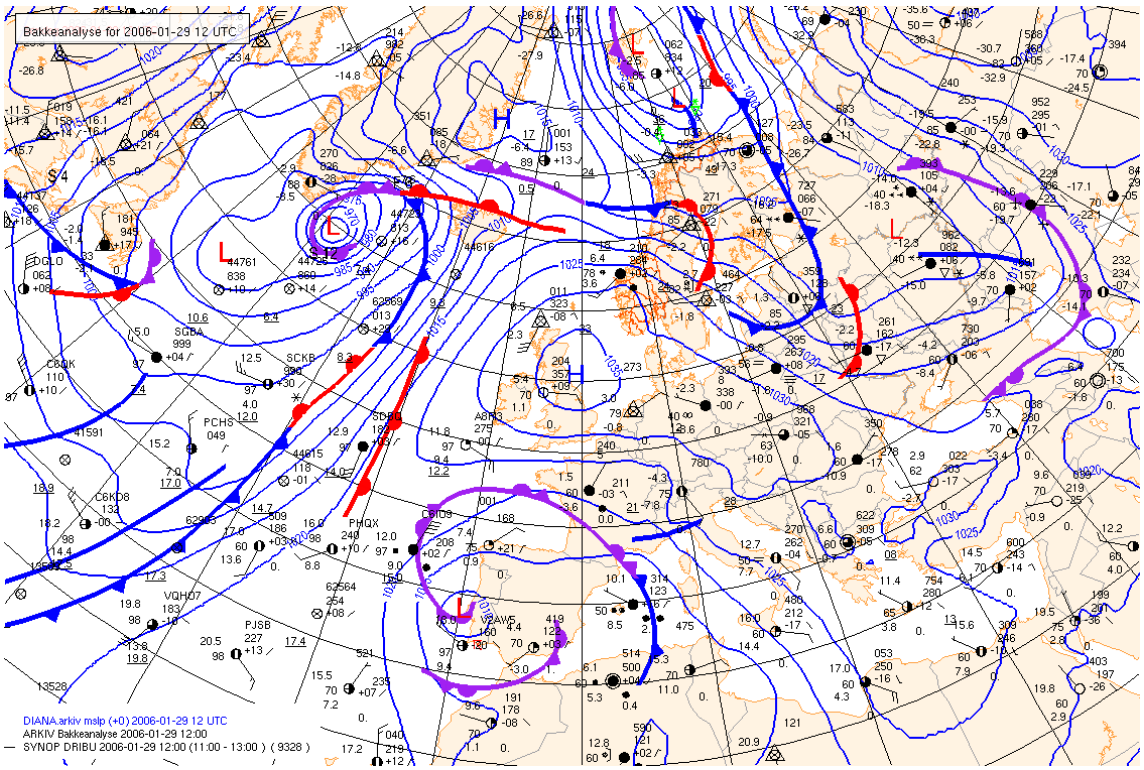

(d) 12 UTC 29 January

Figure A.5

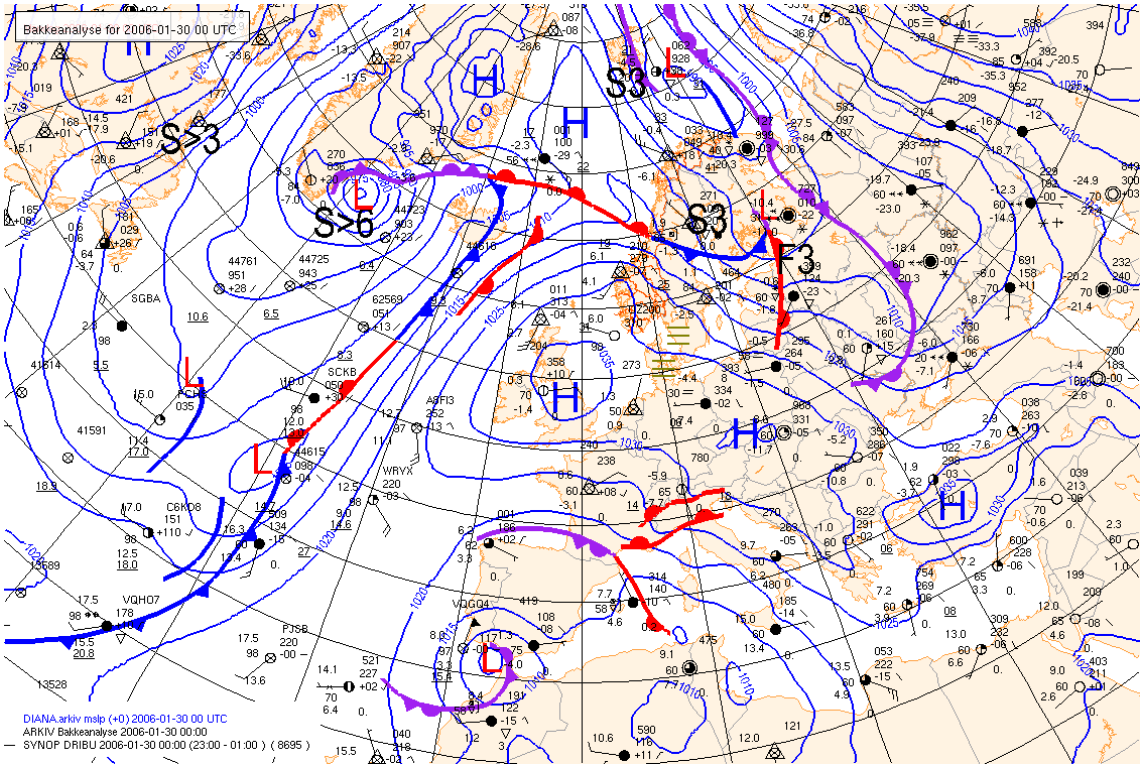

(e) 00 UTC 30 January

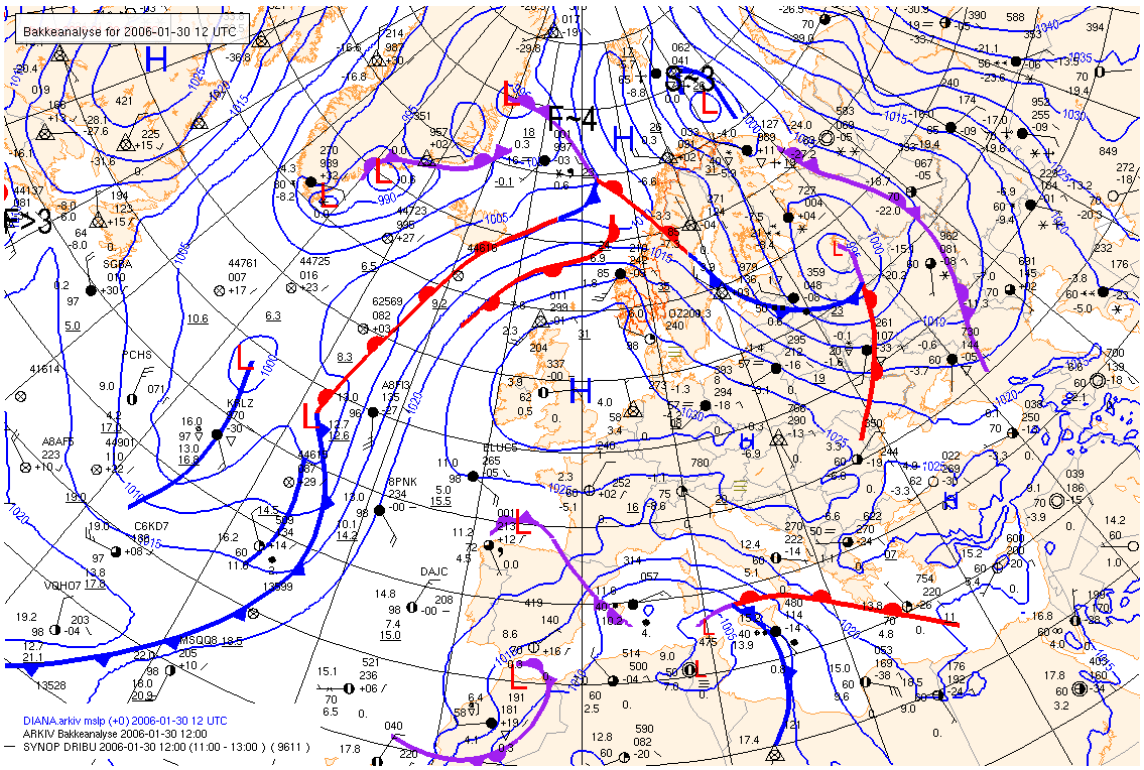

(f) 12 UTC 30 January

Figure A.5

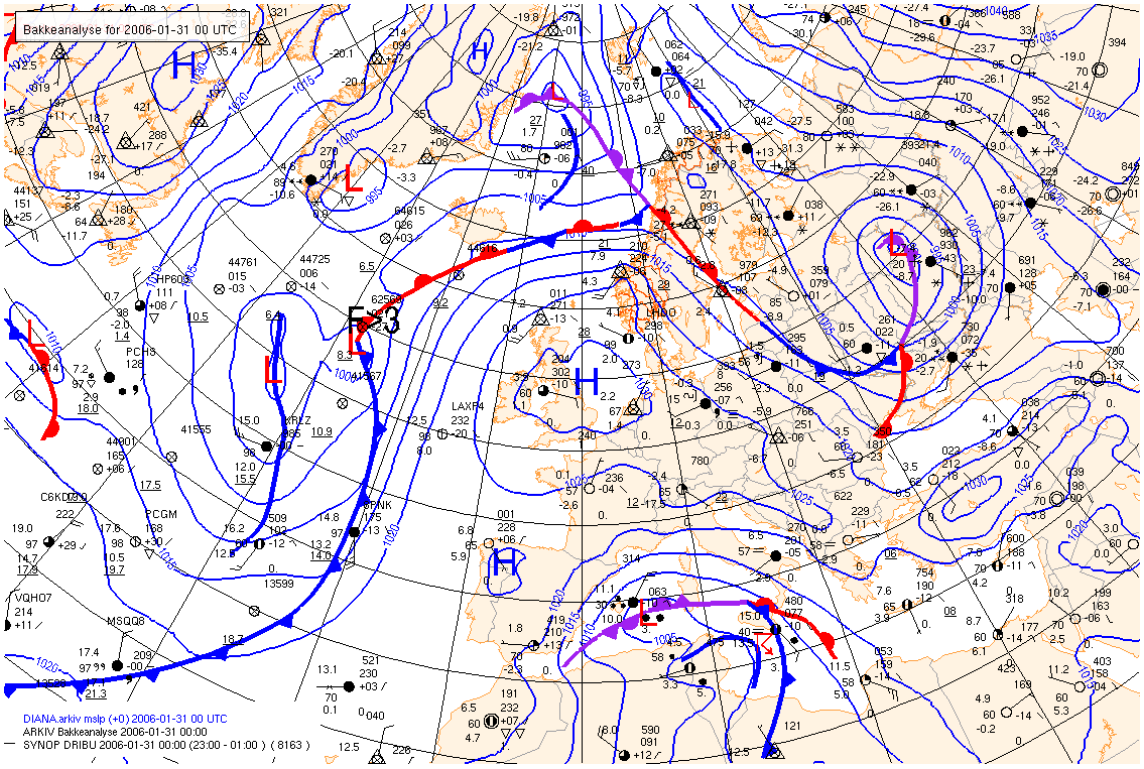

(g) 00 UTC 31 January

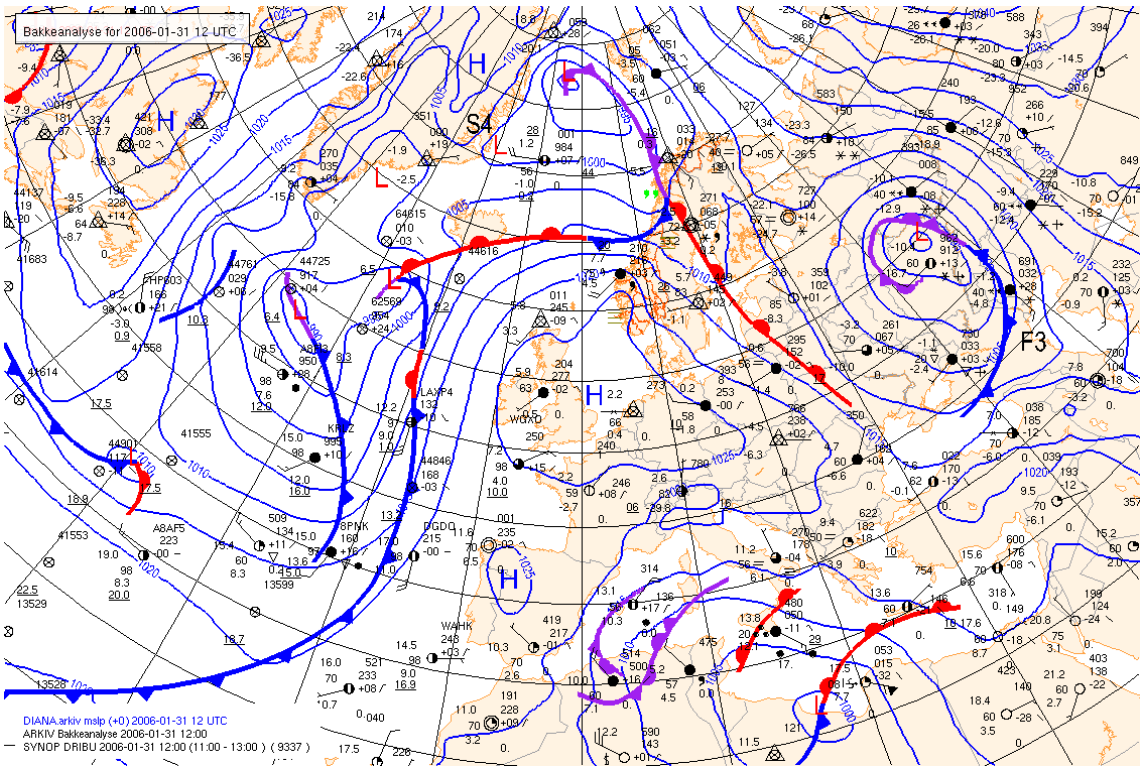

(h) 12 UTC 31 January

Figure A.5

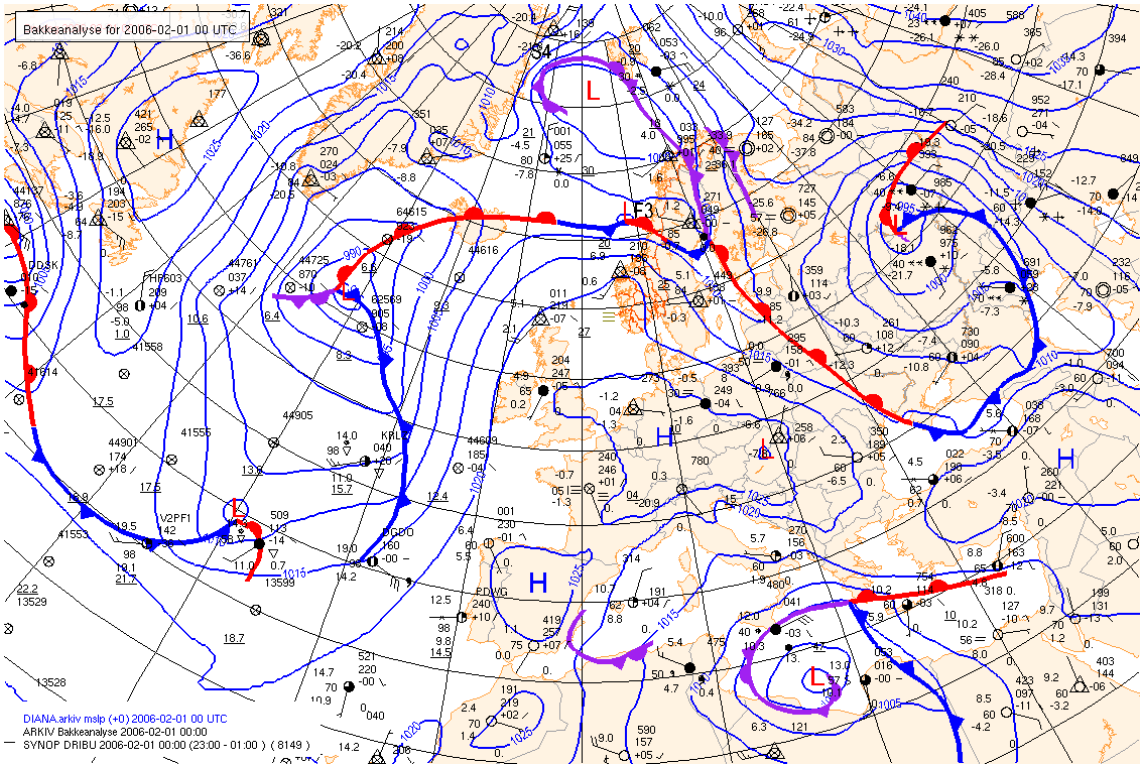

(i) 00 UTC 1 February

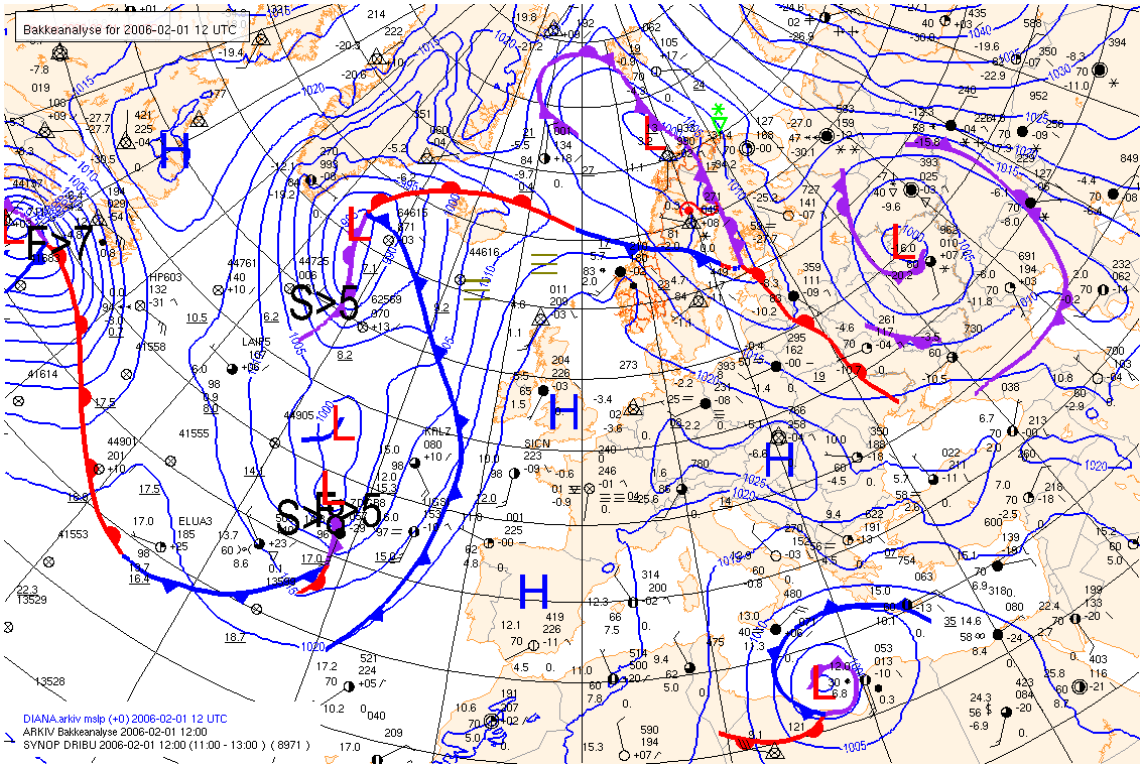

(j) 12 UTC 1 February

Figure A.5

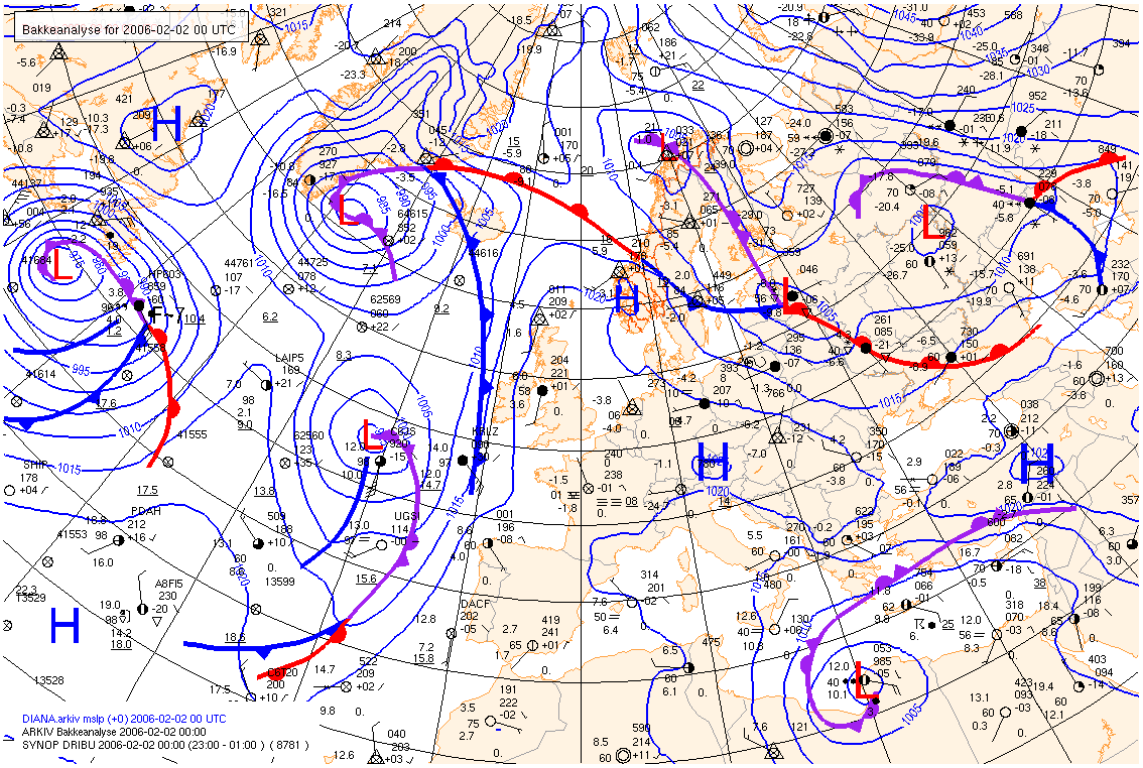

(k) 00 UTC 2 February

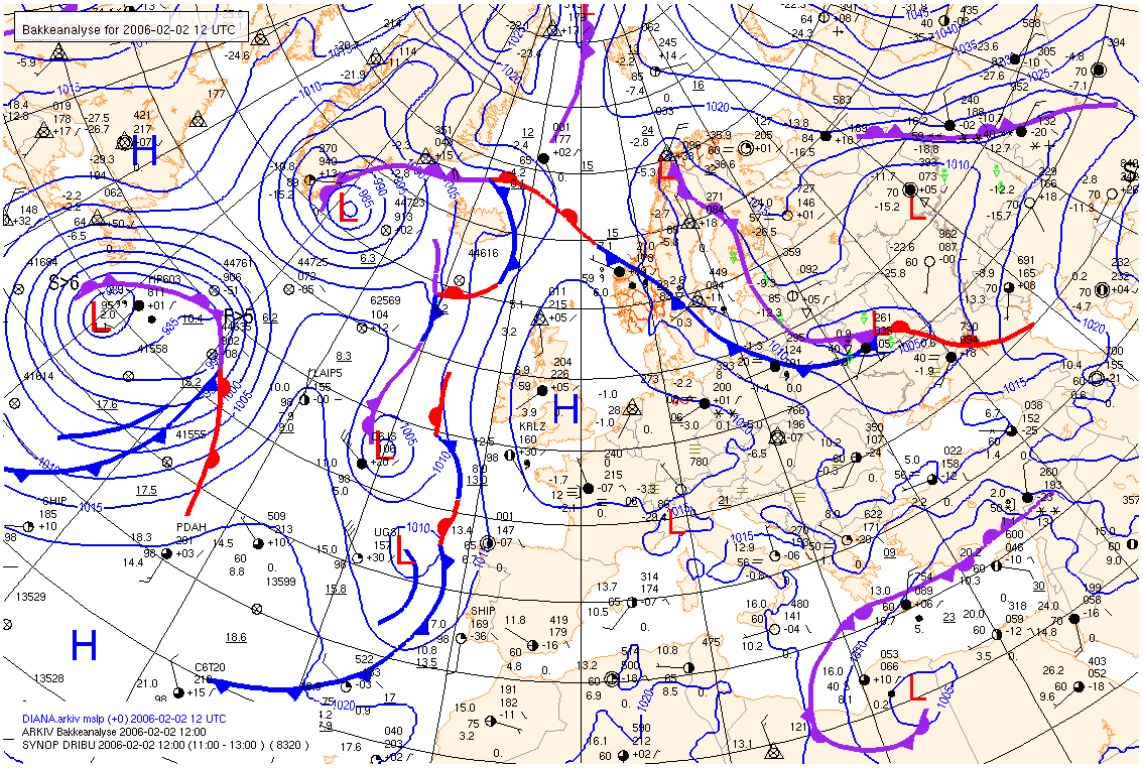

(l) 12 UTC 2 February

Figure A.5: Surface analysis and observations from the Norwegian Meteorological Institution, 5 hPa interval.

Precipitation maps

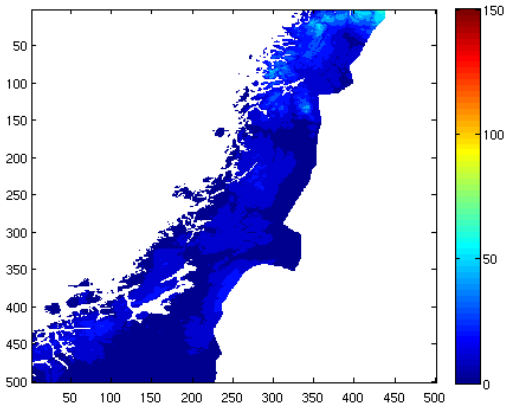

(a) 29 January

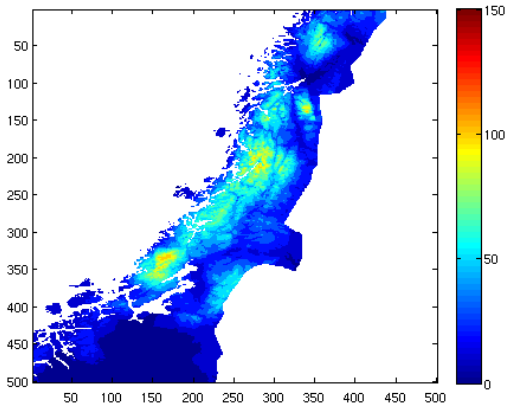

(b) 30 January

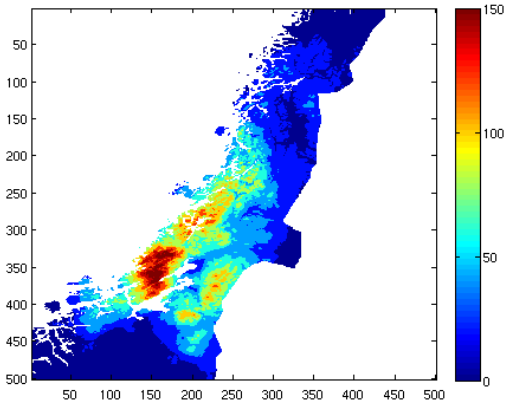

(c) 31 January

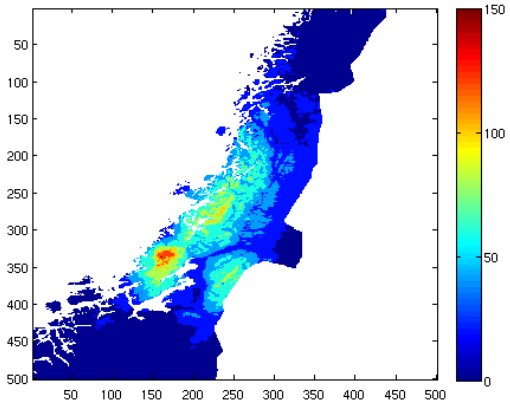

(d) 1 February

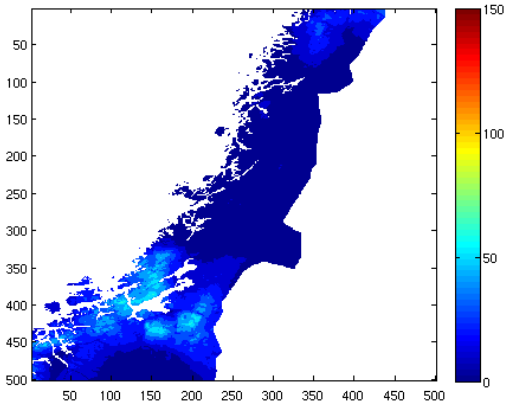

(e) 2 February

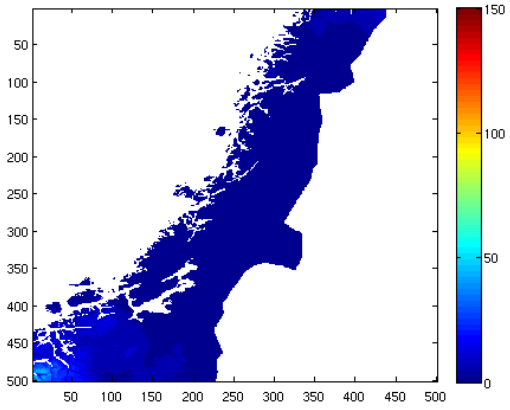

(f) 3 February

Figure A.6: Precipitation maps (mm/24h) over Central Norway (Mohr, 2008).

Bibliography

Alfnes, E., & Førland, E. J. 2006. Trends in extreme precipitation and return values in Norway 1900-2004. *Norwegian Meteorological Institute Report 2/2006.*

Andersson, A., Bakan, S., Fennig, F., Grassl, H., Klepp, C.H., & Schulz, J. 2007. *Hamburg Ocean Atmosphere Parameters and Fluxes from Satellite Data - HOAPS-3 - twice daily composite.* [doi: 10.1594/WDCC/HOAPS3_DAILY].

Beldring, S., Engen-Skaugen, T., Førland, E. J., & Roald, L. A. 2008. Climate change impacts on hydrological processes in Norway based on two methods for transferring regional climate model results to meteorological station sites. *Tellus A*, **60**, 439–450.

Benestad, R. E., & Haugen, J. E. 2007. On complex extremes: flood hazards and combined high spring-time precipitation and temperature in Norway. *Climatic Change*, **85**, 381–406.

Bergeron, T. 1960. Physics of precipitation. *American Geophysical Union, Washington DC, USA.*

Christensenm, J. H., Christensen, O.B., Lopez, P., & van Meijgaard, E. Bolzet, M. 1996. The HIRHAM4 Regional Atmospheric Climate Model. *DMI Scientific Report 96-4. Danish Meteorological Institute.*

Draxler, R. R., & Rolph, G. D. 2010. HYSPLIT (HYbrid Single-Particle Lagrangian Integrated Trajectory) Model access via NOAA ARL READY Website (http://ready.arl.noaa.gov/HYSPLIT.php). *NOAA Air Resources Laboratory, Silver Spring, MD.*

Einarsson, E. M., Ólafsson, H., & Kristjansson, J. E. 2004. Forecasting an extreme precipitation event in Norway. *11th Conference on Mountain Meteorology and the Annual Mesoscale Alpine Program (MAP).*

Elliott, R. D., & Smith, T. B. 1949. A study of the effects of large blocking highs on the General Circulation in the Northern-Hemisphere Westerlies. *Journal of Meteorology*, **6**, 67.

FNO, Finance Norway, Insurance. 2010 (March). *Natural hazzards 1992-2009.*

http://www.fnh.no/PageFiles/17361/Store%20norske%20naturskader%201992-2009.doc.

Hanssen-Bauer, I., & Førland, E.J. 1998. Annual and seasonal precipitation variations in Norway 1896–1997. *KLIMA Report 27:98,Norwegian Meteorological Institute, Oslo.*

Hanssen-Bauer, I., & Førland, E.J. 2000. Temperature and precipitation variations in Norway 1900-1994 and their links to Atmospheric Circulations. *International Journal of Climatology*, **20**, 1693 – 1708.

Hanssen-Bauer, I., & Nordli, P.Ø. 1998. Annual and seasonal temperature variations in Norway 1876–1997. *KLIMA Report 25:98, Norwegian Meteorological Institute, Oslo.*

Hanssen-Bauer, I., Førland, E.J., Haugen, J.E., & Tveito, O. E. 2003. Temperature and precipitation scenarios for Norway: comparison of results from dynamical and empirical downscaling. *Climate Research*, **25**, 15.

Hanssen-Bauer, I., Achberger, C., Benestad, R.E., Chen, D., & Førland, E.J. 2005. Statistical Downscaling of climate scenarios over Scandinavia. *Climate Research*, **29**, 255–268.

Haugen, J. E., & Iversen, T. 2008. Response in extremes of daily precipitation and wind from a downscaled multi-model ensemble of anthropogenic global climate change scenarios. *Tellus Series a-Dynamic Meteorology and Oceanography*, **60**, 411–426.

Hollinger, J. P., Peirce, J. L., & Poe, G. A. 1990. SSM/I Instrument Evaluation. *IEEE transactions on geoscience and remote sensing.*, **28**, 781.

Holton, James R. 2004. *An Introduction to Dynamic Meterology.* 4 edn. Vol. 88. Elsevier Academic press.

Hunt, J. C. R., Ólafsson, H., & Bougeault, P. 2001. Coriolis effects on orographic and mesoscale flows. *Quarterly Journal of the Royal Meteorological Society*, **127**, 601–633.

Hurrell, J. W. 1995. Decadal Trends in the North-Atlantic Oscillation - Regional Temperatures and Precipitation. *Science*, **269**, 676–679.

IPCC. 2001. Climate change 2001: impact, adaption and vulnerability. Summary of policymakers. *WMO, Geneva, Switzerland.*

Jiang, Q., & Smith, R.B. 2003. Cloud timescales and orographic precipitation. *Journal of the Atmospheric Sciences*, **60**, 1543–1559.

Laprise, R. 1992. The Euler equations of motion with hydrostatic pressure as an independent variable. *Monthly Weather Review*, **120**, 197–207.

Mamen, J. 2008. Dypdykk i klimadatabasen, rekorder og kuriositeter fra Meteorologisk institutts klimarakiv. *Naturen*.

Mohr, M. 2008. *New Routines for Gridding of Temperature and Precipitation Observations for "seNorge.no"*. Tech. rept. Norwegian Meteorology Institute.

Ólafsson, H. 2000. The impact of flow regimes on asymmetry of orographic drag at moderate and low Rossby numbers. *Tellus. Series A, Dynamic meteorology and oceanography*, **52**, 365 – 379.

Ólafsson, H., & Bougeault, P. 1996. Nonlinear flow past an elliptic mounatin ridge. *Journal of Atmospheric Sciences*, **53**, 2465–2489.

Pierrehumbert, R. T., & Wyman, B. 1985. Upstream effects of mesoscale mountains. *Journal of the Atmospheric Sciences*, **42**, 977–1003.

Reuder, J., Fagerlid, G. O., Barstad, I., & Sandvik, A. 2007. Stord Orographic Precipitation Experiment(STOPEX): an overview of phase I. *Advances in Geosciences*, **10**, 17–23.

Roeckner, E., Bäuml, G., Bonaventure, L., Brokopf, R., Esch, M., Giorgetta, M., Hagemann, S., Krichner, S., Kornblueh, L., Manzini, E., Rhodin, A., Schlese, U., Schulzweida, U., & Tompkins, A. 2003. The Atmospheric general circulation model ECHAM5, part 1. *Max Planck Institute for Meteorology, report no. 349*.

Rolph, G.D. 2010. Real-time Environmental Applications and Display sYstem (READY) Website (http://ready.arl.noaa.gov). *NOAA Air Resources Laboratory, Silver Spring, MD.*

Skamarock. 2008. A Description of the Advanced Research WRF Version 3. *Ncar technical Note*.

Smith, R. B. 1979. The Influence of Mountains on the Atmosphere. *Advances in Geophysics*, **21**, 87–231.

Smith, R. B. 1989. Mechanisms of Orographic Precipitation. *Meteorological Magazine*, **118**, 85–88.

Spinnangr, F. 1943a. Synoptic studies on precipitation in Southern Norway. I. Instability showers. *Meteorologiske Annaler*, **1**.

Spinnangr, F. 1943b. Synoptic studies on precipitation in Southern Norway. II. Front precipitation. *Meteorologiske Annaler*, **1**.

Spinnangr, F., & Johansen, H. 1954. On the distribution of precipitation in maritime tropical air over Norway. *Meteorologiske Annaler*, **3**.

Stohl, A., Forster, C., & Sodemann, H. 2008. Remote sources of water vapor forming precipitation on the Norwegian west coast at 60°N - a tale of hurricanes and

an atmospheric river. *Journal of Geophysical Research-Atmospheres*, **113**, D05102, doi:10.1029/2007JD009006.

Sumner, E. J. 1954. A study of blocking in the Atlantic-European of the northern hemisphere. *Quarterly Journal of the Royal Meteorological Society*, **80**, 402 – 416.

Ulbrich, U., & Cristoph, M. 1999. A shift in the NAO and increasing storm track activity over Europe due to anthropogenic greenhouse gas forcing. *Climate Dynamics*, **15**, 551–559.

Uvo, C. B. 2003. Analysis and regionalization of northern european winter precipitation based on its relationship with the North Atlantic oscillation. *International Journal of Climatology*, **23**, 1185.

Wentz, F. J. 1997. A well cailbrated ocean algorithm for SSM/I. *Journal of Geophysical Research.*, **102**.

Wentz, F.J., & Spencer, R.W. 1996. *SSM/I Rain Within an Unified All-Weather Ocean Alorithm*. Tech. rept. JAS PIP-2 issue.

Wicker, L. J. 2002. Time-splitting methods for elastic models using forward time schemes. *Monthly Weather Review*, **130**, 2088–2097.